

An Evolution and Eruption of the Coronal Magnetic Field through a Data-Driven MHD Simulation

Satoshi Inoue

Center for Solar-Terrestrial Research, New Jersey Institute of Technology, University Heights, Newark, NJ 07102-1982, USA

Satoshi.Inoue@njit.edu

Keiji Hayashi

George Mason University, 4400 University Dr, Fairfax, VA 22030, USA

Takahiro Miyoshi

Graduate School of Advanced Science and Engineering, Hiroshima University, 1-3-1 Kagamiyama, Higashihiroshima 739-8526, Japan

ABSTRACT

We present a newly developed data-driven magnetohydrodynamics (MHD) simulation code under a zero- β approximation based on a method proposed by Hayashi et al. 2018 and 2019. Although many data-driven MHD simulations have been developed and conducted, there are not many studies on how accurately those simulations can reproduce the phenomena observed in the solar corona. In this study, we investigated the performance of our data-driven simulation quantitatively using ground-truth data. The ground-truth data was produced by an MHD simulation in which the magnetic field is twisted by the sunspot motions. A magnetic flux rope (MFR) is created by the cancellation of the magnetic flux at the polarity inversion line due to the converging flow on the sunspot, which eventually leads the eruption of the MFR. We attempted to reproduce these dynamics using the data-driven MHD simulation. The coronal magnetic fields are driven by the electric fields, which are obtained from a time-series of the photospheric magnetic field that is extracted from the ground-truth data, on the surface. As a result, the data-driven simulation could capture the subsequent MHD processes, the twisted coronal magnetic field and formation of the MFR, and also its eruption. We report these results and compare with the ground-truth data, and discuss how to improve the accuracy and optimize numerical method.

1. Introduction

Active phenomena observed in the solar corona are widely believed to be driven by the coronal magnetic field (Shibata & Magara 2011). Thus, knowledge of how coronal magnetic field evolves from the initial energy through its release is essential to understand these phenomena. The solar flares are one of the most common of these phenomena and are often linked to the origin site of coronal mass ejections (CMEs). CMEs bring lots of coronal gas and magnetic field from the Sun to interplanetary space and cause massive electromagnetic disturbances in the Earth’s magnetosphere when they collide. Therefore, how the coronal magnetic field evolves not only influences the magnetic environment of the solar corona, but also extends this influence to near-Earth space and even to the furthest reaches of the heliosphere.

Magnetic field observations have been conducted by ground and space-based observations which provide us a time-series of the photospheric magnetic field data in high temporal and spatial resolutions. For instance, the solar dynamics observatory (SDO: Pesnell et al. 2012) provides the magnetic field every 12 minutes with a spatial resolution of $0.5''$, which is in Spaceweather HMI Active Patch format (Bobra et al. 2014). In the study of Wang et al. (2017), Goode Solar Telescope (GST: Goode & Cao 2012) at Big Bear Solar Observatory (BBSO) provides magnetic field at $0.08''$ with 87 second cadence. However, the fact that magnetic field is only measured at the photosphere is a technical problem, *i.e.*, three-dimensional (3D) magnetic field is not measured directly. A nonlinear force-free field extrapolation (NLFFF: *e.g.*, Inoue 2016) is one of useful tool, which extrapolates a 3D magnetic field numerically based on the photospheric magnetic field under a force-free approximation. This technique has several achievements, for instance, time variation of the 3D magnetic structure before and after a flare (Schrijver et al. 2008), a formation process of the non-potential magnetic field leading to a solar flare (*e.g.*, Inoue et al. 2011, Sun et al. 2012, Jiang et al. 2014, Woods et al. 2020), and analysis of solar flare onset in terms of time variations of the 3D magnetic fields (*e.g.* Muhamad et al. 2018, Kang et al. 2019, Yamasaki et al. 2021). However, the NLFFF extrapolation only provides one snapshot of the magnetic field bounded by the force-free assumption and the essential problems still remain. For instance, the photospheric magnetic field used as the boundary condition cannot satisfy the force-free state (Metcalf et al. 1995, Kawabata et al. 2020a) and there is no guarantee of a unique solution under the given boundary and initial conditions (Kawabata et al. 2020b).

Although the NLFFF gives a snapshot of 3D magnetic field at specific time, a data-constrained magnetohydrodynamic (MHD) simulation, which uses the potential field, NLFFF and non-force-free field as the initial conditions, can cover the evolution and dynamics of the magnetic field that is freed from an assumption of the equilibrium state (*e.g.*, Inoue 2016,

Muhamad et al. 2017, Inoue et al. 2018, Jiang et al. 2018, Prasad et al. 2020, Nayak et al. 2021). The data-constrained MHD simulation uses only one snapshot vector magnetic field. According to Inoue et al. (2018), the normal component of the photospheric magnetic field is fixed with time and the time-dependent horizontal magnetic fields are derived from the induction equation, so that the evolution of the tangential components is not exactly consistent with the time-series of the photospheric magnetic field. Nevertheless, these simulations reproduce the observations quantitatively, such as distribution of the flare ribbons and erupting direction of the magnetic flux rope (*e.g.*, Inoue et al. 2014, Jiang et al. 2017, Muhamad et al. 2017).

A data-driven MHD simulation drives the coronal magnetic field where a time-series of the photospheric magnetic field is applied to the boundary condition (Toriumi et al. 2020, Jiang et al. 2022). This method is more advanced than the data-constrained MHD simulation. The problem is how to treat the boundary condition, *i.e.*, how to treat the induction equation at bottom boundary. Note that we consider very simple situation under zero- β approximation without taking into account the time-varying density and pressure at the bottom surface. The induction equation is written as follows in an ideal MHD framework,

$$\frac{\partial \mathbf{B}}{\partial t} = -\nabla \times \mathbf{E} = \nabla \times (\mathbf{v} \times \mathbf{B}), \quad (1)$$

where \mathbf{B} , \mathbf{E} and \mathbf{v} are magnetic field, electric field, and plasma velocity, respectively. From Eq.(1), we have several ways to drive the coronal magnetic field above, for instance, the electric field is given at the bottom boundary (Fisher et al. 2010, Fisher et al. 2020, Kazachenko et al. 2014, Lumme et al. 2017, Hayashi et al. 2018). \mathbf{E} has gauge invariance *i.e.*, it should be described as $\mathbf{E} = \mathbf{E}_I + \nabla\phi$ which implies that the given electric field and the evolution of the coronal magnetic field depend on the gauge invariance. Nevertheless, Cheung & DeRosa (2012), Pomoell et al. (2019) and Price et al. (2020) reproduced various observational features by choosing the gauge with ingenuity. For example, Pomoell et al. (2019) compares the magnetic field lines with the Extreme Ultraviolet (EUV) images and Price et al. (2020) superimposes the field lines on the images for a more rigorous comparison. The structure of the magnetic field lines is in good agreement with the structure of the magnetic field lines inferred from the images. Furthermore, Cheung & DeRosa (2012) reproduced the back reaction of the eruption that enhances the photospheric magnetic field after the eruption. Recently, Kaneko et al. (2021) derived the photospheric velocity by inversely solving the induction equation by imposing physical constraints on the gauge and driving the coronal magnetic field using the obtained velocity. Several methods directly give either the magnetic field or velocity, or both in their data-driven simulation despite both the magnetic field and the velocity are given at the boundary conditions is an over-specification for an MHD. For example, the velocity is derived from the algorithm of Differential Affine Velocity Estimator

for Vector Magnetogram (DAVE4VM:Schuck 2008). Although the detailed method is different for each, they have produced a non-potential magnetic field prior to the flare or the eruption of the MFR well (Jiang et al. 2016, Leake et al. 2017, Liu et al. 2019, Guo et al. 2019, Hayashi et al. 2019, Jiang et al. 2021).

Recently, Hayashi et al. (2018) and Hayashi et al. (2019) proposed a new method for the data-driven MHD simulation in which three electric fields are defined at the bottom boundary, and a half-grid above and below that completely reproduce the photospheric magnetic field through the induction equation. Hayashi et al. (2019) includes a data-driven simulation in which the coronal magnetic field is driven by the velocity. Following their method, the velocity, which is obtained from DAVE4VM, is given on the bottom surface while the magnetic field is driven by the velocity through the MHD process. Their simulation was applied to solar active region (AR) 11158 and reproduced the evolution toward the non-potential magnetic field starting with the potential field. Eventually the magnetic fields prior to the flare were obtained, which were similar to coronal magnetic fields inferred from the EUV observations. In this study we develop a data-driven MHD code based on the method proposed by Hayashi et al. (2018) . The code is designed with a zero- β approximation because the magnetic pressure is dominant over the gas pressure in the lower solar corona, and constructed using a finite-differential method based on Inoue et al. 2014. The purpose of this study is to test the accuracy of this data-driven MHD simulation to compare with the ground-truth data including evolution of the coronal magnetic fields during the energy buildup and eruption process. Leake et al. (2017) and Toriumi et al. (2020) discussed accuracy of the data-driven simulations by comparison to the ground-truth data. Leake et al. (2017) examined the sensitivity of data-driven simulation results to the cadence of the input boundary driving-data maps. In their study, all MHD variables are given at the bottom-boundary. They found that the cadence is indeed important for reproducibility. Toriumi et al. (2020) compares the simulation results from the participating data-driven simulation models. In their comparison, the models are given only the information on the boundary magnetic field at a low cadence and yield very different solutions from the ground-truth solution. Our electric field driven model uses only the information on the solar-surface magnetic field. Therefore, our newly developed code also needs the accuracy test.

From the two aforementioned works, in this present study, the target ground-truth three-dimensional solution and the bottom-boundary time-dependent magnetic field data maps would be prepared with the same MHD code but driven with variables other than magnetic field. We followed the velocity-driven MHD model procedures by Amari et al. (2000) and Amari et al. (2003) for generating the ground-truth solutions and the time-dependent magnetic-field data maps. This ground-truth data includes the eruption of the magnetic field which is different from previous works by Leake et al. (2017) and Toriumi et

al. (2020).

Note that the electric field obtained from the inversion of the induction equation is not uniquely determined due to the uncertainty of the gauge, hence it is not guaranteed that the electric field will indeed reproduce the evolution of the magnetic field in the ground-truth data produced by velocity-driven MHD. In addition, the electric-field inversion is designed to utilize only (temporal difference of) the magnetic field data on the bottom boundary surface at two consecutive sampling instants. In other word, the method in Hayashi et al. (2018) is not designed to accommodate information on the temporal evolution of the ground-truth magnetic field or the three-dimensional structure in the whole volume. Given these caveats above, it is crucially important to assess how well the electric field-driven MHD models using the electric-field inversion can yield the ground-truth solution. In this work, we quantitatively evaluate the results of the data-driven MHD simulation by comparing with the ground-truth data. We further discuss the numerical treatment of implementation method, for which intrinsically we are allowed to make somewhat arbitrary choice in, for example, spatial differencing.

The rest of this paper is constructed as follows. The numerical method is described in section 2. The results and discussion are presented in section 3 and section 4. Finally, our conclusion are summarized in section 5.

2. Numerical Method

2.1. Basic Equations

We solve the following zero- β MHD equation to make the ground-truth data and also conduct the data-driven simulation,

$$\frac{\partial \rho}{\partial t} = -\nabla \cdot (\rho \mathbf{v}) + \zeta \nabla^2 \rho, \quad (2)$$

$$\frac{\partial \mathbf{v}}{\partial t} = -(\mathbf{v} \cdot \nabla) \mathbf{v} + \frac{1}{\rho} \mathbf{J} \times \mathbf{B} + \nu \nabla^2 \mathbf{v}, \quad (3)$$

$$\frac{\partial \mathbf{B}}{\partial t} = \nabla \times (\mathbf{v} \times \mathbf{B}) + \eta \nabla^2 \mathbf{B} - \nabla \phi, \quad (4)$$

$$\mathbf{J} = \nabla \times \mathbf{B}, \quad (5)$$

$$\frac{\partial \phi}{\partial t} + c_h^2 \nabla \cdot \mathbf{B} = -\frac{c_h^2}{c_p^2} \phi, \quad (6)$$

where \mathbf{B} is the magnetic flux density, \mathbf{v} is the velocity, \mathbf{J} is the electric current density, ρ is the pseudo density, and ϕ is the convenient potential to remove errors derived from $\nabla \cdot \mathbf{B}$ (Dedner et al. 2002), respectively. ρ_0 corresponds to the initial density. The length, magnetic field, density, velocity, time, and electric current density are normalized by L^* , B^* , ρ^* , $V_A^* \equiv B^*/(\mu_0 \rho^*)^{1/2}$, where μ_0 is the magnetic permeability, $\tau_A^* \equiv L^*/V_A^*$, and $J^* = B^*/\mu_0 L^*$. ν and η are viscosity and resistivity, fixed by 1.0×10^{-3} and 1.0×10^{-5} , respectively, and the coefficients c_h^2 , c_p^2 in Eq.(6) also fix the constant value, 0.04 and 0.1, respectively. ζ is a diffusion coefficient of the density which avoids the sudden variation of the density to improve the robustness of the simulation, where ζ is set to 1.0×10^{-4} in this study. A numerical box of $1.0 \times 1.0 \times 1.0$, which is given in its non-dimensional value, is divided by $320 \times 320 \times 320$ grid points.

2.2. Ground-truth data

We first make ground-truth data according to an MHD simulation done by Amari et al. (2000) and Amari et al. (2003) to verify the reproducibility of the energy storage and release processes of the coronal magnetic field by our data-driven MHD simulation. We first set a simple bipole magnetic field like sunspots as shown in Fig.1a, from which the potential field is extrapolated in the 3D space following the Green function method (Sakurai 1982) as shown in Fig.1b. The initial velocity and density are set as $|\mathbf{v}| = 0.0$ and $\rho_0 = 1.0$ in the whole space, respectively.

Next we impose a twisting motion on the photosphere according to,

$$\mathbf{v}_h^{(b)}|_{z=0} = (v_x, v_y) = \left(-\frac{\partial \psi}{\partial x}, \frac{\partial \psi}{\partial y} \right), \quad (7)$$

where ψ is a stream function which satisfies $\mathbf{v}_h^{(b)}|_{z=0} = \mathbf{z} \times \nabla_h \psi$. We give ψ the following formula,

$$\psi(x, y, t) = \gamma(t) \{B_z^{(b)}\}^2 e^{\left\{ \frac{-(B_z^{(b)})^2 - (B_{z:max}^{(b)})^2}{(B_{z:max}^{(b)})^2} \right\}},$$

and

$$\gamma(t) = -0.5 \tanh \left\{ 2.0 \frac{(t - t_{cri}) - 1.0}{0.5} \right\} + 0.5,$$

where $B_z^{(b)}$ and $B_{z:max}^{(b)}$ correspond to the magnetic field measured at the photosphere and the maximum value, respectively. If time t is beyond the critical time set at t_{cri} where we set

$t_{cri} = 9.0$, $\gamma(t)$ quickly falls to zero. The twisting motion is shown in Fig.1c. It is convenient to give ψ as a function of B_z because the twisting motion is imposed along the contour of B_z , *i.e.*, $(\mathbf{v}_h \cdot \nabla)B_z = 0$ is promised regardless of B_z . Thus the distribution of B_z will not be changed by the twisting motion. Since we assume $v_z=0$ at the bottom surface as well as $(\mathbf{v}_h \cdot \nabla)B_z = 0$, these conditions satisfy $\partial_t B_z = 0$. Therefore, normal flux is not transported across the bottom surface during the evolution and our simulation can keep $\int \mathbf{B} \cdot d\mathbf{S} = 0$. When $\gamma(t)$ falls to zero, the twisting motion at the photosphere comes to a complete halt. Afterward, the magnetic field is relaxed for a while, *i.e.*, no external motion is imposed. The horizontal magnetic components B_x and B_y at the photosphere are following the equations during the twisting motion and relaxation process after the twisting motion is over,

$$\begin{aligned}\frac{\partial B_x^{(b)}}{\partial t} &= - \left(\frac{\partial E_z}{\partial y} - \frac{\partial E_y}{\partial z} \right) - \frac{\partial \phi}{\partial x}, \\ \frac{\partial B_y^{(b)}}{\partial t} &= - \left(\frac{\partial E_x}{\partial z} - \frac{\partial E_z}{\partial x} \right) - \frac{\partial \phi}{\partial y},\end{aligned}\tag{8}$$

while B_z is fixed. E_x and E_y represent the electric field in x and y components which are described as $(-\mathbf{v} \times \mathbf{B}) \cdot \mathbf{x}$ and $(-\mathbf{v} \times \mathbf{B}) \cdot \mathbf{y}$, respectively. The v_z and density ρ are fixed with initial value at the bottom boundary and ϕ is imposed on the Neumann condition throughout the simulation. Note that, during the relaxation process, E_z at the bottom surface is zero, *i.e.*, $\partial_x E_z = \partial_y E_y = 0$ because the evolutions of v_x and v_y are halted there ($v_x = v_y = 0$).

Finally, after the relaxation, we impose a diverging motion on the sunspot, which corresponds to a converging motion around the PIL, as shown in Fig.1d. The diverging motion is given as the following formula (*e.g.*, Xia et al. 2014),

$$\begin{aligned}v_x^{(b)} &= - \frac{\partial |B_z^{(b)}|}{\partial x} e^{\left\{ \frac{-(x-0.5L_x)^2}{x_d^2} \right\}}, \\ v_y^{(b)} &= - \frac{\partial |B_z^{(b)}|}{\partial y} e^{\left\{ \frac{-(y-0.5L_y)^2}{y_d^2} \right\}},\end{aligned}\tag{9}$$

where $x_d=y_d=0.1$ is given. The magnetic field at the bottom boundary follows an induction equation in each component as below,

$$\begin{aligned}\frac{\partial B_x^{(b)}}{\partial t} &= - \left(\frac{\partial E_z}{\partial y} - \frac{\partial E_y}{\partial z} \right) + \eta \frac{\partial^2 B_x^{(b)}}{\partial x^2} - \frac{\partial \phi}{\partial x}, \\ \frac{\partial B_y^{(b)}}{\partial t} &= - \left(\frac{\partial E_x}{\partial z} - \frac{\partial E_z}{\partial x} \right) + \eta \frac{\partial^2 B_y^{(b)}}{\partial x^2} - \frac{\partial \phi}{\partial y}, \\ \frac{\partial B_z^{(b)}}{\partial t} &= - \left(\frac{\partial E_y}{\partial x} - \frac{\partial E_x}{\partial y} \right) + \eta \frac{\partial^2 B_z^{(b)}}{\partial x^2} - \frac{\partial \phi}{\partial z},\end{aligned}\tag{10}$$

note that the diffusion is given in the direction of converging motion (in this study, it corresponds to x direction) to make the simulation more robust. This diverging motion is continuously imposed on the sunspot until the end of the simulation. In both cases, twisting motion and diverging motion, we normalized the velocity $\mathbf{v}^{(b)}$ by the maximum value $|v_{y:max}^{(b)}|$ and multiplied by 0.01, *i.e.*, $\mathbf{v}^{(b)} \Rightarrow 0.01\mathbf{v}^{(b)}/|v_{y:max}^{(b)}|$, before being used in Equations (8) and (10), so that the maximum absolute value of the velocity is set as 0.01 at the bottom surface.

2.3. Data-driven Simulation

2.3.1. Three Electric Fields Driving the Coronal Magnetic Field

In this study, a data-driven MHD simulation is performed according the method proposed by Hayashi et al. (2018) and Hayashi et al. (2019). We will now briefly describe this method. In this method the coronal magnetic field is driven by electric fields given at the bottom. In order to determine the electric fields that derive the time evolving observed photospheric magnetic field through an induction equation, three types of electric fields are assumed to satisfy the following induction equations,

$$\frac{\partial B_z}{\partial t} = -\mathbf{z} \cdot \nabla \times \mathbf{E}^{(1)}, \quad (11)$$

$$\frac{\partial \mathbf{B}_{h:df}}{\partial t} = -\nabla \times \mathbf{E}^{(2)}, \quad (12)$$

$$\frac{\partial \mathbf{B}_{h:cf}}{\partial t} = -\nabla \times \mathbf{E}^{(3)}, \quad (13)$$

where the horizontal field (\mathbf{B}_h) at the photosphere is decomposed into $\mathbf{B}_{h:df}$ and $\mathbf{B}_{h:cf}$, *i.e.*, $\mathbf{B}_h = \mathbf{B}_{h:df} + \mathbf{B}_{h:cf}$ where these satisfy $\nabla_h \cdot \mathbf{B}_{h:df} = 0$ and $\nabla_h \times \mathbf{B}_{h:cf} = 0$, respectively.

Following Hayashi et al. (2018), three Poisson equations are derived from the above three induction equations. First, when $\mathbf{z} \cdot \nabla \times$ is multiplied by the first induction equation (11), the first Poisson equation is obtained as follows,

$$\nabla^2 \Phi^{(1)} = -\frac{\partial B_z}{\partial t}, \quad (14)$$

where we make the following assumption, $\mathbf{E}^{(1)} = \mathbf{z} \times \nabla \Phi^{(1)}$, *i.e.*, $\partial E_z^{(1)}/\partial z = 0$. Since the right hand side of Eq.(14) can be calculated from the photospheric magnetic field, we can solve the Eq. (14) under an appropriate boundary condition and obtain $\mathbf{E}^{(1)}$ to determine B_z at the photosphere.

The second Poisson equation is

$$\begin{aligned}\nabla^2\Phi^{(2)} &= -\mathbf{z} \cdot \left(\nabla \times \frac{\partial \mathbf{B}_{h:df}}{\partial t} \right) \\ &= -\mathbf{z} \cdot \left(\nabla \times \frac{\partial \mathbf{B}_h}{\partial t} \right),\end{aligned}\tag{15}$$

where $\mathbf{E}^{(2)} = -\mathbf{z}\Phi^{(2)}$ is assumed. The advantage of this assumption is that it does not change the normal component of the magnetic field at the photosphere because it is determined by $E_x^{(1)}$ and $E_y^{(1)}$. Namely, if we further give $E_x^{(2)}$ and $E_y^{(2)}$, B_z changes and deviates from the observation. This assumption is able to avoid the conflict of B_z being obtained from $\mathbf{E}^{(1)}$ and $\mathbf{E}^{(2)}$. The detailed derivation process of Eq.(15) is described in Appendix (A.1).

The third Poisson equation is

$$\begin{aligned}\nabla_h^2\Phi^{(3)} &= \frac{1}{2}\Delta z \nabla_h \cdot \left(\frac{\partial \mathbf{B}_{h:cf}}{\partial t} \right) \\ &= \frac{1}{2}\Delta z \nabla_h \cdot \left(\frac{\partial \mathbf{B}_h}{\partial t} \right),\end{aligned}\tag{16}$$

where Δz is the grid interval and we make the following assumption, $\mathbf{E}^{(3)}|_{z=+\frac{1}{2}\Delta z} = \mathbf{z} \times \nabla_h \Phi^{(3)}$. Note that since B_z is perfectly derived from $E_x^{(1)}$ and $E_y^{(1)}$, $\mathbf{E}^{(3)}$ is an over condition to determine B_z . Therefore, $\mathbf{E}^{(3)}$ is defined at locations half-grid above and below the photosphere as follows,

$$\mathbf{E}^{(3)}|_{z=+\Delta z/2} = -\mathbf{E}^{(3)}|_{z=-\Delta z/2}.\tag{17}$$

$\Phi^{(3)}$ is defined at the plane half-grid above the bottom surface but it is determined by given horizontal magnetic field at the bottom surface, so Δz plays the role of the bridge between the left and right handed values defined at each different height. The detailed derivation process of Eq.(16) is described in Appendix (A.2). Eventually, we obtain $\mathbf{E}^{(1)}$, $\mathbf{E}^{(2)}$ and $\mathbf{E}^{(3)}$ through the three Poisson equations (14), (15) and (16). The positional relationship of the three electric fields is summarized in Fig.2.

2.3.2. How to drive the magnetic field at the bottom surface

The magnetic field at the bottom surface is driven by $\mathbf{E}^{(1)} = (E_x^{(1)}, E_y^{(1)}, 0)$, $\mathbf{E}^{(2)} = (0, 0, E_z^{(2)})$ and $\mathbf{E}^{(3)} = (E_x^{(3)}, E_y^{(3)}, 0)$ where $\mathbf{E}^{(1)}$ and $\mathbf{E}^{(2)}$ are defined at the bottom surface while $\mathbf{E}^{(3)}$ is defined one half-grid above (and also below) the bottom surface. Note that, following Hayashi et al. (2018), $\mathbf{E}^{(1)}$ is also placed at the surface one half-grid above (and also below) the bottom, taking into account conservation of the normal flux. The different

from $\mathbf{E}^{(3)}$ is that we assume $\mathbf{E}_{z=+\Delta z/2}^{(1)} = \mathbf{E}_{z=-\Delta z/2}^{(1)}$, so its z derivative becomes zero. This positional relationship is represented in Fig.2. The time derivative of B_z is written as

$$\frac{\partial B_z}{\partial t} = - \left(\frac{\partial E_y^{(1)}}{\partial x} - \frac{\partial E_x^{(1)}}{\partial y} \right), \quad (18)$$

and since $\mathbf{E}^{(2)}$ only has a z -component, $\mathbf{B}_{h:df}$ is described as

$$\frac{\partial \mathbf{B}_{h:df}}{\partial t} = \left(-\frac{\partial E_z^{(2)}}{\partial y}, \frac{\partial E_z^{(2)}}{\partial x} \right), \quad (19)$$

where all the components are defined in x and y components, thus we omit the z component. Regarding the time derivative of $\mathbf{B}_{h:cf}$, by taking into account the assumption of $\mathbf{E}^{(3)}$, $E_z^{(3)}$ equals to zero and $\mathbf{E}^{(3)}$ is defined as the plane half-grid above and below the bottom surface. The x -component of $\partial_t \mathbf{B}_{h:cf}^{(3)}$ is written as

$$\begin{aligned} \left(\frac{\partial B_{x:cf}^{(3)}}{\partial t} \right)_{z=0} &= \frac{\partial E_y^{(3)}}{\partial z} \\ &= \frac{E_y^{(3)}|_{+\Delta z/2} - E_y^{(3)}|_{-\Delta z/2}}{\Delta z} \\ &= \frac{2}{\Delta z} E_y^{(3)}, \end{aligned}$$

similarly,

$$\left(\frac{\partial B_{y:cf}^{(3)}}{\partial t} \right)_{z=0} = -\frac{2}{\Delta z} E_x^{(3)},$$

where the details are described in the Appendix of Hayashi et al. (2018). Therefore,

$$\begin{aligned} \frac{\partial B_x}{\partial t} &= - \left(\frac{\partial E_z^{(2)}}{\partial y} - \frac{2}{\Delta z} E_y^{(3)} \right), \\ \frac{\partial B_y}{\partial t} &= - \left(-\frac{\partial E_z^{(2)}}{\partial x} + \frac{2}{\Delta z} E_x^{(3)} \right), \\ \frac{\partial B_z}{\partial t} &= - \left(\frac{\partial E_y^{(1)}}{\partial x} - \frac{\partial E_x^{(1)}}{\partial y} \right), \end{aligned} \quad (20)$$

are given at the bottom surface.

2.4. Numerical method of the data-driven simulation

The same MHD equations (Eq.(2)-Eq.(6)) are applied to the data-driven MHD simulation while the electric fields, $\mathbf{E}^{(1)-(3)}$ are given at the bottom and a half-grid above and below as shown in Fig.2. Since the location that is one grid above the bottom ($k=1$ shown in Fig.2) corresponds to the practical bottom boundary, the derivation of the magnetic field at this position ($k=1$) is important for the data-driven simulation in this study. Especially, the derivative in z direction introduced in the induction equation should be handled with care because it includes the difference between non-MHD components ($\mathbf{E}^{(1)}$ and $\mathbf{E}^{(3)}$) which are placed at $k=0$ or $1/2$ and the electric fields obtained from MHD process ($-\mathbf{v} \times \mathbf{B}$) which are placed at $k=2$.

According to a second order finite differential method, the derivative of E in the z -direction at $k=1$ in the induction equation is written as,

$$\begin{aligned} \frac{\partial E}{\partial z} \Big|_{k=1} &= \frac{E_{k=2} - E_{k=0}}{2\Delta z}, \\ &= \frac{E_{k=2} - E_{k=1}}{2\Delta z} + \frac{E_{k=1} - E_{k=0}}{2\Delta z}, \\ &= \frac{E_{k=2} - E_{k=1}}{2\Delta z} + \left(\frac{E_{k=1} + E_{k=0}}{2\Delta z} \right) - \frac{2E_{k=0}}{2\Delta z}, \\ &= \frac{E_{k=2} - E_{k=1}}{2\Delta z} + \left(\frac{E_{k=\frac{1}{2}}}{\Delta z} - \frac{E_{k=0}}{\Delta z} \right), \end{aligned}$$

where E is either the x or y component and we use the following approximation,

$$E_{k=\frac{1}{2}} = \frac{E_{k=1} + E_{k=0}}{2\Delta z}, \quad (21)$$

to obtain the last equation. When we take into account $E_{k=\frac{1}{2}} = E^{(1)} + E^{(3)}$ and $E_{k=0} = E^{(1)}$, we obtain

$$\frac{\partial E}{\partial z} \Big|_{k=1} = \frac{E_{k=2} - E_{k=1}}{2\Delta z} + \frac{E^{(3)}}{\Delta z}. \quad (22)$$

On the other hand, we can write down the different formula as follows,

$$\begin{aligned} \frac{\partial E}{\partial z} \Big|_{k=1} &= \frac{E_{k=2} - E_{k=0}}{2\Delta z}, \\ &= \frac{E_{k=2} + E_{k=1}}{2\Delta z} - \frac{E_{k=1} + E_{k=0}}{2\Delta z}, \\ &= \frac{E_{k=2} + E_{k=1}}{2\Delta z} - \frac{E_{k=\frac{1}{2}}}{\Delta z}, \end{aligned}$$

where $E_{k=\frac{1}{2}}$ is approximated in Eq.(21). Eventually, we obtain the following equation,

$$\frac{\partial E}{\partial z}|_{k=1} = \frac{E_{k=2} + E_{k=1}}{2\Delta z} - \frac{E^{(1)} + E^{(3)}}{\Delta z}. \quad (23)$$

Hereafter, the former written in Eq.(22) is denoted as Type-A and the later (Eq.(23)) is denoted as Type-B. We will mainly show the results obtained from Type-A and discuss the difference in results between Type-A and Type-B.

The coronal magnetic fields is driven as outlines in Fig. 3. We derive the electric field $\mathbf{E}^{(1)-(3)}$ at each time interval from the two output data at t_n and t_{n+1} ($n=1,2,3,\dots$) obtained from the referenced MHD simulation where only the magnetic field at the bottom is used. The time interval $t_{n+1} - t_n$ is set to 0.5625. The electric fields are derived from the three Poisson equations (14), (15) and (16). In this study, we use the Gauss-Seidel method to solve them. The performance and convergence of the Poisson equations are shown in Appendix (see Fig.A1). In the data-driven simulation, each electric field drives the upper coronal magnetic field at each interval. Note that, in this study, we drive the coronal magnetic field when the $|\mathbf{B}| = \sqrt{B_x^2 + B_y^2 + B_z^2}$ measured at the bottom is more than 0.0625, *i.e.*, the weak magnetic field region does not change with time.

As seen in Table-1, we ran 8 different simulations which are mainly classified into the cases of TW and the cases of CV where TW and CV mean data-driven simulations in twisting (phase energy buildup phase: $t=0\sim 11.25$ in the MHD simulation) and the converging phase (energy released phase: $t\geq 22.5$ in the MHD simulation), respectively. The initial conditions of the data-driven MHD simulations in the cases of TW and CV employ the magnetic fields at $t=0$ and $t=22.5$ obtained from the ground-truth data. Note that the data-driven simulations are not conducted continuously from $t=0$ to after the eruption. Because one of objectives of this study is that how the data-driven simulation can produce the energy release phase. If we conduct the data-driven simulation from $t=0$ to the eruption, it becomes difficult to isolate whether the errors are due to the energy buildup phase ($t=0-11.5$) or the relaxation phase ($t=11.5-22.5$). We focus on evaluating the data-driven simulation in the energy buildup phase without the extra errors. The Type-A and -B differential methods denote -A (A0, A1, and A2), and -B, respectively. The Type-A is further classified into A0, A1, and A2 where the vertical velocity (v_z) placed at one grid ($k = 1$) above the bottom surface has been given through a specific update in the temporal evolution and the method is different in each case. In the cases of A1 and A2, the vertical velocity (v_z) is fixed to zero or is update through a linear interpolation with values of $k = 0$ and $k = 2$, respectively, while the A0 has no specific updated, *i.e.*, the vertical velocity is derived from an equation of motion directly. In case B, we run one simulation where the vertical velocity at $k = 1$ is updated using the liner interpolation.

3. Results

3.1. Overview of Ground-truth Data

The temporal evolution of the magnetic and kinetic energies are shown in Fig.4. Both energies are buildup by $t \sim 11.25$ due to the twisting motion of the sunspot, then gradually decrease by $t \sim 22.5$ in the relaxation phase. Note that the twisting motion is halted at $t \sim 11.25$ and the magnetic fields are relaxed by $t \sim 22.5$. Within a few moments of turning on the converging motion at $t \sim 22.5$, the kinetic energy increases dramatically, whilst the magnetic energy decreases a lot of which is dissipated and converted into the Joule heating through the flux cancellation.

The evolution of the 3D magnetic field lines, while the twisting motion is imposed, is shown in Fig.5. As time passes, the magnetic field lines are sheared gradually and eventually a sigmoidal structure is formed at $t=10.12$ which is often observed prior to flares (*e.g.*, Savcheva et al. 2012, Inoue et al. 2012, Kawabata et al. 2018).

After the relaxation, we impose the diverging flow on the sunspots as shown in Figs.6a-c with the evolution of the sunspots. From the upper panels, a part of the magnetic flux is transported toward the polarity inversion line (PIL) at which they are canceled. The lower panels (Figs.6d-e) show the evolution of the magnetic field lines. The footpoints of the magnetic field lines are carried by the flow on the both sunspots and field lines of opposite polarity encounter each other at the PIL. Magnetic reconnection then takes place, resulting in the formation of the long and highly twisted lines as seen in Figs.6e and f. The continuous converging flow around the PIL enhances the further twisted MFR and lifts it upward as seen in Fig.7b where the magnetic field lines just before the diverging flow are imposed are shown in Fig.7a. The current sheet is formed under the lifted MFR and eventually it erupts as shown in Figs.7c and d.

We have attempted to reproduce these MHD processes by using the data-driven MHD simulation in which the electric field works as the driving source on the bottom surface, instead of the velocity field. These electric fields are derived from a time series of the magnetic field on the bottom surface of the ground-truth data produced by the MHD simulation.

3.2. Results of the Data-driven MHD Simulation

3.2.1. Energy Buildup Phase

First, we show the results of data-driven simulation in energy buildup phase in which the ground-truth data shows the formation of Sigmoid. The initial condition of the data-driven simulation was given by the potential magnetic field shown in Fig.1b and the time-dependent electric fields are given at bottom and one-half the above (and also below). Figures 8a and b show the temporal evolution of the magnetic and kinetic energies, respectively. From Fig.8a, we can see that the temporal evolutions of magnetic energies in the data-driven simulations are almost indistinguishable to each other. It should also be noted that the quantities from the data-driven simulations are very similar to the initial ground-truth data, but as the evolution continuous they deviate from this. Note that free magnetic energy is essential to discuss the eruption rather than the net magnetic energy shown in this study. However, the potential field is exactly same in the ground-truth and data-driven simulations because the bottom B_z is exactly same between them. Therefore, the profile of the free magnetic energy is same to the one shown in Fig.5(a) while the magnitudes differ between the net magnetic energy and free magnetic energy. From Fig.8b, although the kinetic energy increases in the temporal evolution in both the ground-truth data and each data-driven simulation, the behaviors are slightly different among them. We note that the kinetic energy is much smaller than the magnetic energy.

The temporal evolution of the 3D magnetic field obtained from the data-driven simulation (TW-A02) is shown in Fig.9 . The data-driven simulation reproduces a similar evolution to the ground-truth data as shown in Fig.5. In particular, the sigmoidal structure is reproduced well in the final time-step. On the other hand, the sheared field lines accumulated in the data-driven simulation look weaker than those in the ground-truth data. Nevertheless, this result shows that the data-driven simulation works well.

We show more quantitative results by using magnetic twist defined as

$$T_w = \int \frac{\nabla \times \mathbf{B} \cdot \mathbf{B}}{|\mathbf{B}|^2} dl, \quad (24)$$

where dl is a line element of each field lines (Berger & Prior 2006). Fig.10a shows the temporal evolution of the magnetic flux in the ground-truth data and each case of the data-driven simulation. These magnetic flux are stored by the magnetic field lines which satisfy a condition $T_w \leq -0.1$. Although the magnetic flux, which is composed of the non-potential component, obtained from the data-driven simulation is a bit smaller than the magnetic flux obtained from the MHD simulation, the behavior is almost same among them. Fig.10b shows the histogram of the magnetic flux which depends on the twist value for the ground-

truth and data-driven simulation (TW-A02). Although the twist value obtained from the data-driven simulation is slightly weaker than that calculated from the ground-truth data, the two distributions are very similar. The distributions of the magnetic twist of each field line are mapped on the each surface. The results calculated from the ground-truth data and the data-driven MHD (TW-A02) simulation are also very similar as seen in Figs.10c and d. Thus, these results support that the data-driven simulation reproduces the twisting process of the magnetic field lines well.

3.2.2. Energy Release Phase

Next we show the results obtained from the data-driven MHD simulation in the energy release phase. This corresponds to the erupting phase of the MFR formed by the converging motion. The initial condition of the data-driven simulation was given by the magnetic field at $t = 22.5$ of the ground-truth data. Figs.11a and b show the temporal evolutions of the magnetic and kinetic energies obtained from the ground truth and data-driven simulations. We can see that the magnetic and kinetic energies obtained from the data driven simulations capture the tendency to decrease and increase as is seen in the respective ground truth data. However, in the case CV-A0 the kinetic energy grows very slowly compared to other cases, which will be discussed later.

As seen in Fig.A3, the bottom B_z obtained from the data-driven simulation reproduces the ground-truth data well. The correlation coefficient is over 0.99 at each time. This means that the potential fields extrapolated from the bottom B_z of the ground-truth data and obtained from the data-driven simulation are almost identical. Although the magnitudes of the net magnetic energy and free magnetic energy are different from each other, the behavior is the same as that shown in Fig.11(a).

The temporal evolution of the 3D magnetic field lines in the case of CV-A2 is shown in Fig.12. The MFR is formed through the converging motion which is driven by the electric field, and causes an eruption, under which the current sheet is enhanced. We confirmed that the evolving 3D magnetic field shown in the data-driven simulation is consistent with the ground-truth data, thus the data-driven simulation looks to work well in the energy release process of the magnetic field that corresponds to the erupting phase of the MFR.

The results of the quantitative analysis (especially focusing on the case of CV-A2) are shown in Fig.13. Figure 13a shows the temporal evolution of the magnetic flux, which is dominated by the highly twisted field lines, $|T_w| \geq 1.0$, in each case where these highly twisted field lines are newly created during the evolution. The evolution obtained from the

data-driven simulation in each case almost captures the ground-truth data (black) while the growth in the case of CV-A0 is very slow as inferred from the result shown in Fig.11b. Figure 13b represents a histogram for the magnetic flux vs. magnetic twist for the ground-truth data and data-driven simulation (CV-A2). Figs.13c and d show the distribution of the T_w mapped on the surface, obtained from the ground-truth data and the data-driven simulation (CV-A2), respectively. Although these do not match exactly, both are very similar. Thus we confirmed that the data-driven simulation works well in terms of the quantitative analysis.

We trace the magnetic axis of the MFR in the evolution for the ground-truth data and the data-driven MHD simulations, respectively. In this study, we detect the axis at which the sign of B_x inverts along the center of the numerical box which corresponds to the dashed vertical line as shown in Fig.14a. Because the symmetry of the MFR is well during the evolution. Figure 14b plots the field lines on the vertical cross section (x-z plane) and the red circle points out the same position shown in Fig.14a which corresponds to a center of the MFR. The temporal evolutions of the MFR axis of the ground-truth data and those obtained from each case of the data-driven simulation are shown in Fig.14c. Although case CV-A0 deviates from the result from the ground-truth data, other cases obtained from the data-driven simulations capture its behavior well. Therefore, the data-driven simulation developed in this study, which is based on Hayashi et al. (2018), can be used as a powerful tool to understand the evolution of the coronal magnetic field and the physics of solar eruptions.

4. Discussion

4.1. Why is a special update required for the vertical velocity located at $z = \Delta z$?

In above section, we found that the case of CV-A0 does not capture the ground-truth data well, for instance, in the temporal evolution of the kinetic energy and the axis of the MFR. One other notable difference when compared to the other cases from the data-driven simulation is that the eruption occurs later in the CV-A0 case. The difference between these cases is the handling of the vertical velocity (v_z) at $k = 1$, *i.e.*, $z = \Delta z$. Therefore, we should examine the behavior of the vertical velocity at $z = \Delta z$ or around the position, in both energy build up and energy release phases, respectively.

Figure 15 shows the temporal evolutions of the velocity field obtained from the ground-truth data and the data-driven MHD simulation (TW-A0 and TW-A2), respectively, at the surface at $z = 3\Delta z$. Although the horizontal velocity plotted by the arrows forms a twisting motion in each case, the vertical velocity (v_z) distributions are quite different. The most

striking difference is that the negative vertical velocity appears in late phase of the data-driven MHD simulations. So, we hereafter discuss the spacial and temporal evolutions of the vertical velocity.

Figure 16 shows the temporal evolutions of the vertical velocity along the center of the numerical box, *i.e.*, the vertical dashed line as shown in Fig.14a, which are obtained from ground-truth data and the data-driven simulations, respectively, in the energy buildup phase (TW-A0 to TW-A2). For the ground-truth data, the velocity temporally increases according to the twisting motion given on the photosphere. Although the vertical velocity in TW-A1 and TW-A2 increases as times goes on, it enhances the negative value with time in the region close to the solar surface, which is different to the ground-truth data. The typical result is the case of TW-A0 in which the velocity is negatively increased close to the solar surface with time. The small inset is an enlarged view in the height range 0 to 0.01. We found that the velocity located at one grid above the bottom surface, *i.e.*, $z = \Delta z$, is fastest way to enhance the negative value. The time variation of the vertical velocity in the case of TW-A0 is determined by the equation of motion while in TW-A1 it is set of zero and TW-A2 it is updated by a linear interpolation in the vertical direction, respectively. Either the convective term $\mathbf{v} \cdot \nabla \mathbf{v}$ or Lorentz force $\mathbf{J} \times \mathbf{B}$, or both would have a negative influence on the vertical velocity. Despite each velocity profile begins different in each case of energy buildup phase, magnetic energy is found to follow almost the same behavior in each case (Fig.8) . Since the magnetic energy is dominant over the kinetic energy, the evolution of the magnetic field is almost unaffected by the velocity field, conversely a small fluctuation of the magnetic field would greatly influence the evolution of the velocity. Therefore, the Lorentz force would be a major factor inhibits the vertical velocity from leading the correct solution. Note that, in the real situation, since no one can say that the magnetic energy dominates and the velocity field does not affect the magnetic evolution much on the photosphere, the situation is expected to become more complex.

Figure 17 plots the temporal evolution of the vertical velocity in the energy release phase, *i.e.*, the erupting phase of the MFR in the same format as in Fig.16. The data-driven simulations, CA-V1 and CA-V2 capture the ground-truth data well while the results obtained from CV-A0 show the different behavior. From the small inset follows the same format as in Fig.16b, the value at $z = \Delta z$ suddenly becomes the negative value. This behavior is the same as seen in the case of TW-A0 in the energy buildup phase. However, this case differs from TW-A0 in that the velocity recovers from its negative value during the late phase.

Figures 18a and b compare the temporal evolutions of the vertical velocity located at $z = \Delta z$ for the ground-truth data and the results obtained from between the data-driven simulation in energy buildup phase (TW-A0 and TW-A2) and energy release phase (CV-

A0 and CV-A2). Note that the vertical velocity at $z = \Delta z$ for the cases of TW-A1 and CV-A1 is set to zero, so we exclude these plots. The TW-A2 and CV-A2 cases somewhat capture the ground-truth data, while cases TW-A0 and CV-A0 show large deviations from the ground-truth by exhibiting a steep drop in the negative value from the initial values. CV-A0 however is found to increase the velocity back towards that seen in the ground-truth data. It is likely that when the magnetic field is converted into the dynamics phase from the static phase, the strong positive enhancement of the velocity is associated with the eruption, which returns to the ground-truth data even at $z = \Delta z$.

As seen in these results, we need a careful treatment of the vertical velocity at $z = \Delta z$ in the static phase, which is found to largely deviate from the ground-truth data without the treatments. Since the kinetic energy in the energy buildup phase is much smaller than the magnetic energy, the evolution of the magnetic field is unaffected by the velocity field even if the velocity strongly deviates from the ground-truth data as seen in Fig. 8. On the other hand, it affects the initiation of the eruption, which causes delays because the down flow, which is an unlikely result in the ground-truth data, inhibits local reconnection at the photosphere and therefore the formation of the MFR. Thus, some treatments (simple linear interpolation was applicable in this study) would be required.

Why does the vertical velocity (v_z) located at $z = \Delta z$ show different behaviors in each case? From the above results, when the difference to the ground-truth data is striking, the magnetic field evolves in the quasi statical energy buildup phase toward the pre-erupting stage. Since the magnitude of the kinetic energy is much lower than the magnetic energy in the energy buildup phase, $\mathbf{J} \times \mathbf{B}$ is the major factor to lowering velocity. Each component of the Lorentz force (\mathbf{F}) is described as

$$F_x = J_y B_z - J_z B_y,$$

$$F_y = J_z B_x - J_x B_z,$$

$$F_z = J_x B_y - J_y B_x,$$

where B_z at $z = \Delta z$ is derived from the rotation of the electric fields located at $z = \Delta z$ while a derivative of E_y and E_x in z component is included to derive the B_x and B_y , respectively, according to equation (22). B_z is determined by $E_{k=1}$ which is derived from MHD electric field ($-\mathbf{v} \times \mathbf{B}$) while B_x and B_y are derived from $E_{k=2}$, $E_{k=1}$ and $E^{(3)}$ too (see Equation (22)). $E_{k=2}$ and $E_{k=1}$ are different from $E^{(3)}$ because the $E^{(3)}$ is derived from a non-MHD process. Therefore, the z -derivative is generally not allowed at $z = \Delta z$ and the physical consistency regarding of the obtained B_x and B_y is not guaranteed. F_z includes more B_x and B_y than the other components F_x and F_y , so the value of v_z that is derived from F_z will have a lesser accuracy.

4.2. What is difference between Type-A and Type-B?

We now discuss results obtained from the data-driven simulation for the case of TW-B that implements a differential method type-B described in equation (23). We first compare with the results obtained from the ground-truth data. Figures.19a and b plot the temporal evolutions of the magnetic and kinetic energies in the energy buildup phase, *i.e.*, the magnetic field is twisted due to the photospheric motion. Both evolutions obtained from the data-driven simulation shows large deviations from the ground-truth data. Figures 19c, d, and e show the distribution of $|\mathbf{J}|/|\mathbf{B}|$ plotted on the vertical cross section for the ground-truth data and the data-driven MHD simulations (TW-A2 and TW-B), respectively, from which the TW-A2 case reproduces the ground-truth data well, while the case of TW-B shows a totally different solution.

The difference between the TW-A2 and TW-B is the application of differing numerical differential methods, especially, at $z = \Delta z$ at $k = 1$. The derivative forms in the z direction for each are as follows, with type-A written as

$$\frac{\partial E}{\partial z}\Big|_{k=1} = \frac{1}{2} \left[\frac{E_{k=2} - E_{k=1}}{\Delta z} + \left(\frac{E_{k=\frac{1}{2}} - E_0}{\frac{\Delta z}{2}} \right) \right], \quad (25)$$

and type-B is written as

$$\frac{\partial E}{\partial z}\Big|_{k=1} = \frac{\frac{(E_{k=2} + E_{k=1})}{2} - E_{k=\frac{1}{2}}}{\Delta z}. \quad (26)$$

Type-A is an average value of the central differential method of electric fields obtained from the MHD process (the first term in the right hand side of Eq.(25)) and non-MHD process (the second term). Although each derivative has physical meaning, there is a discrepancy between the MHD term and non-MHD term. The use of the average process in this case smoothly connects them, making a more robust calculation. Type-B is a central differential method of the electric fields obtained from the MHD and non-MHD processes. In principle, this derivative is not allowed as discussed in above section because the origin of those electric fields is different, *i.e.*, there are not connected smoothly. Therefore, this discrepancy might negatively impact the simulation result.

On the other hand, Hayashi et al. (2018) and Hayashi et al. (2019) implement type-B and the simulation works well. One reason for the difference in results from this study is the difference in the numerical schemes used. Hayashi et al. (2018) and Hayashi et al. (2019) are designed with the finite volume method, and numerical viscosity and resistivity might efficiently work on the negative impact and make the simulation stable. However, such viscosity and resistivity do not work efficiently in the central differential method as used in this study despite these being included explicitly in the induction equation and the equation

of motion. Therefore, numerical instability is not suppressed in this study and the solution is not reproduced correctly as seen in Fig.19e.

4.3. Dependency on Time Cadence

We test the effect on the accuracy of our results to the time cadence used in the data-driven MHD simulations used in this study. Figure 20a shows the comparison of the temporal evolution of the kinetic energies in the energy buildup phase that is obtained from the ground-truth data, the data-driven simulation (TW-A2), and a new data-driven simulation with 2.5 times the temporal resolution ($t_{n+1} - t_n = 0.225$) of TW-A2 (TW-A2D). These are plotted in black, red, and blue, respectively. Since the blue line almost overlaps with the red line, no significant differences due to the temporal evolution are apparent in the energy buildup phase. Thus we can say that the solution is convergent with respect to temporal resolution.

Figure 20b shows the each kinetic energy during the energy release phase, plotted in the same format as Fig. 20a. The red line, which corresponds to the data-driven simulation (CV-A2), diverges slightly from the blue line (CV-A2D) that has 2.5 times the temporal resolution of CV-A2. This difference is from the result in the energy buildup phase. However, the difference between CV-A2 and CV-A2D is only a few percent. From these results, our solution is almost convergent in temporal resolution. According to Leake et al. (2017), using a higher temporal cadence makes the results of a data-driven simulation closer to the ground-truth data. However, we do not see this in our results. One of possible reason could be due to differences in the methods used to create the simulation. Leake et al. (2017) directly uses data that are extracted from the ground-truth data where-as our method drives the coronal magnetic field by electric fields given near the solar surface that are derived from the bottom magnetic fields of the ground-truth data. It is therefore likely that these differing methods are the reason for the differing effect to adjusting the temporal resolution of the simulation.

Furthermore, it is important to consider a ratio of the sampling time (dt_s) to the dynamical time (dt_d) proposed by Leake et al. (2017) and the ratio should be less than 1. The dynamical time is defined by $dt_t = \Delta/V_p$ where Δ is a length of the grid interval and V_p is velocity of the photosphere. In this study, since $\Delta = 1/320$ and maximum $V_{p(max)} = 0.01$, $dt_{t(min)}$ is given as 0.3125. The sampling time dt_s is given as 0.5625 (low time resolution cases) and 0.225 (high time resolution cases,), therefore the ratio corresponds to 1.8 and 0.72, respectively. The ratio in the low time resolution cases (other than TW-A2D and CV-A2D) is over 1. However, in this work, the bottom-boundary parameters driving the system are from a model and thoroughly given in form of functions of time and position. From this

reason, there is little uncertainty in the boundary data (sampling data) and there is not much difference in energies between the low time resolution cases and high time resolution cases.

4.4. Data-driven Simulation through the Energy Accumulation Process to the Release Process

We run the data-driven simulation throughout the entire process from the energy accumulation process to the release process. The result is shown in Fig. 21(a) in which the temporal evolution of the ground-truth data and the data-driven simulation is plotted in black and red, respectively. We found that the data-driven simulation cannot cause the eruption that is different from the results discussed above. One of possible reasons is the pre-erupting magnetic field. Figures 21(b) and (c) show the pre-erupting magnetic fields of the ground-truth data and produced by the data-driven simulation, respectively. The size of the sigmoidal structure is different between them. Fig. 10(b) shows the magnetic flux of the pre-erupting magnetic fields that depends on the twist value before the relaxation process. From this result, the maximum twist value of the ground-truth data is in a range from 0.6 to 0.7. On the other hand, the highly twisted field lines buildup in the data-driven simulation are concentrated approximately up to $T_w=0.6$. This may be very small to cause the eruption. For instance, Inoue et al. (2018) suggested that to cause the solar flares associated with the eruptions requires the twisted field lines with twist values from 0.5 to 1.0. Therefore, the ground-truth data does not have much of twist and it would be difficult for the magnetic field produced by the data-driven simulation to cause the eruption. This result indicates that a little difference in twist may affect the eruption. Furthermore, this is a reminder of that the 3D solution is not uniquely determined even using same boundary condition.

Although the problem may be caused by the ground-truth data that has weakly twisted field lines before the eruption in this study, we should avoid the problem of weakening of the twist of the magnetic field lines produced in the data-driven simulation when using the photospheric magnetic field. The NLFFF would be useful as the initial condition of the data-driven simulation before the eruption. Because, in some cases, the NLFFF before the eruption reproduces more highly twisted field lines than those shown in Fig. 21(c) (Inoue 2016). However more discussion is needed on the issue of whether to use the magnetic field produced in the data-driven simulation or the NLFFF as the initial condition. This would be addressed in future work.

5. Summary

The three-dimensional coronal magnetic field plays an essential role in producing solar phenomena such as solar flares, solar jets, and CMEs. However, the 3D coronal magnetic field is not fully understood as only observations of the photospheric magnetic field can currently be made. Data-driven simulations (Toriumi et al. 2020) are a powerful tool to detect not only the 3D magnetic structure but also chart its evolution. However an important question about their reliability still remain. Therefore, in this study, we developed a new data-driven MHD code based on Hayashi et al. (2018) which is designed with a zero-beta approximation and a central differential method, and confirmed its performance. In order to check the performance of the developed data-driven MHD simulation code, we carried out a benchmark test using ground-truth data made from a time evolving 3D magnetic field produced in the MHD simulation (Amari et al. 2000 and Amari et al. 2003). This covers the typical subsequent evolution from the energy buildup stage to the erupting stage, as seen in a flare productive active region (Toriumi & Wang 2019). Leake et al. (2017) and Toriumi et al. (2020) tested the accuracy of their data-driven simulations using the ground-truth data that was made from flux emergence simulations. In this study, our ground-truth data includes the erupting process of the MFR. Consequently, we confirmed that our data-driven simulation can reproduce the erupting processes of the magnetic field well.

We found that if there are no any treatments for the vertical velocity (v_z) at $z = \Delta z$, the temporal evolution deviates strongly from the ground-truth data. This is inferred from the discrepancy due to a derivative in the z derivation of the electric field which includes MHD electric field ($-\mathbf{v} \times \mathbf{B}$) and non-MHD electric field ($E^{(3)}$). In this study, we found that simple linear interpolation or rather v_z set to zero better suppresses the deviation from the original MHD solution. We found that these deviations are larger when the magnetic field evolves in quasi static energy buildup process toward the eruption. After the eruption, we found that the vertical velocity returns towards the values seen in the ground truth data. There are no remarkable differences between the magnetic field evolutions, which are obtained from the data-driven simulations, in the energy buildup phase even though the vertical velocity at $z = \Delta z$ in each case is not the same way. However, from Fig.11b, the initiation of the MFR eruption is later than other cases obtained from the data-driven simulation if the vertical velocity does not behave correctly. This result suggests that the down-flow, which is unlikely in the ground-truth data, inhibits reconnection at the photosphere and hence the formation of the MFR (see Fig.13a). Therefore, we require the treatment of the vertical velocity at $z = \Delta z$.

There are several choices for the discretization methods applied at $z = \Delta z$ which is practical boundary condition of the method proposed in Hayashi et al. (2018). The critical

issue is the derivative in the z direction between the electric fields obtained from the MHD and non-MHD processes. This is because, in general, this derivative is not allowed and that contradiction causes the numerical instability. We suggested that the stability strongly depends on the numerical scheme used. In addition, we here note that the vertical size of the simulation grid (Δz) can be arbitrarily determined in the simulation setup; therefore, changing Δz can be a remedy to reduce the differences in the simulation results of type A and B. We will investigate this point further in the future.

In this study, we found that our data-driven simulation could capture an overview of the evolution of the 3D coronal magnetic field which mimics the evolution as seen in flare productive active region. As a next step, we will apply the observed photospheric magnetic field to our data-driven simulation code. In general, there is no guarantee that the success of this simulation will result in the success of this future simulation. For example, in this study, we assigned enough spatial resolution to the PIL where the converging motion drives the eruption. Although it is important to correctly capture the photospheric motion near the PIL for the eruption, some observational data do not provide that. Recently, large ground-telescopes such as the GST at BBSO and the Daniel K. Inouye Solar Telescope (Rast et al. 2021) provide high resolution data, which will be helpful in resolving this issue. To use these high resolution data, we will need further optimization and implement further technical upgrades in our code. Additionally, in this study, we did not take into account v_z at the bottom surface in the ground-truth data as in Leake et al. (2017) and Toriumi et al. 2020, so we have not estimated how much this velocity effects the data-driven simulation. However, we believe that our data-driven simulation has potential to reproduce the evolution of the magnetic field from the energy buildup stage to its erupting stage even using observed magnetic field based on its performance in this study.

We are grateful to a referee for constructive comments and Dr. Magnus Woods for reading this paper. This work was supported by the National Science Foundation under grant AGS-1954737, AGS-2145253 and National Aeronautics and Space Administration under grant 80NSSC21K1671. This work was also supported by the computational joint research program of the Institute for Space-Earth Environmental Research, Nagoya University. KH is supported by National Aeronautics and Space Administration under grants 80HQTR20T0067. TM is supported by JSPS KAKENHI Grant Numbers JP20K11851 and JP20H00156. The visualization was done using VAPOR (Clyne & Rast 2005, Clyne et al. 2007).

Appendix

A. Derivation of the Poisson Equations

A.1. Derivation of the Second Poisson Equation for $\Phi^{(2)}$

First we multiply $\nabla_h \cdot$ by equation (12), then

$$\nabla_h \cdot (\nabla \times \mathbf{E}^{(2)}) = -\frac{\partial}{\partial z} \left(\frac{\partial E_y^{(2)}}{\partial x} + \frac{\partial E_x^{(2)}}{\partial y} \right) = 0,$$

should be satisfied at the boundary. If we assume

$$\mathbf{E}^{(2)} = -z\Phi^{(2)}, \quad (\text{A1})$$

the above relationship is satisfied. We substitute Eq.(A1) to Eq.(12), then we can obtain

$$-\nabla \times \mathbf{E}^{(2)} = -\nabla \times (-z\Phi^{(2)}) = \left(\frac{\partial \Phi^{(2)}}{\partial y}, -\frac{\partial \Phi^{(2)}}{\partial x}, 0 \right).$$

Therefore, we describe the equation for $\mathbf{B}_{h:df}$ as follows,

$$\frac{\partial \mathbf{B}_{h:df}}{\partial t} = \left(\frac{\partial \Phi^{(2)}}{\partial y}, -\frac{\partial \Phi^{(2)}}{\partial x}, 0 \right). \quad (\text{A2})$$

We multiply $\nabla \times$ and its z component corresponds to the second Poisson equation (Eq.15),

$$\begin{aligned} \nabla^2 \Phi^{(2)} &= -z \cdot \left(\nabla \times \frac{\partial \mathbf{B}_{h:df}}{\partial t} \right) \\ &= -\left\{ \frac{\partial}{\partial x} \left(\frac{\partial B_{y:df}}{\partial t} \right) - \frac{\partial}{\partial y} \left(\frac{\partial B_{x:df}}{\partial t} \right) \right\} \\ &= -\left\{ \frac{\partial}{\partial x} \left(\frac{\partial B_y}{\partial t} \right) - \frac{\partial}{\partial y} \left(\frac{\partial B_x}{\partial t} \right) \right\}. \end{aligned}$$

Since the right-handed term can be derived from the observed B_x and B_y , we can find $\Phi^{(2)}$ and eventually obtain $\mathbf{E}^{(2)}$ through the equation(A1). Note that we used

$$\frac{\partial}{\partial x} \left(\frac{\partial B_{y:cf}}{\partial t} \right) - \frac{\partial}{\partial y} \left(\frac{\partial B_{x:cf}}{\partial t} \right) = 0.$$

A.2. Derivation of the Third Poisson Equation for $\Phi^{(3)}$

The solenoidal condition, $\nabla \cdot \mathbf{B} = 0$ can be rewritten as follows,

$$\nabla \cdot \mathbf{B}_h + \frac{\partial B_z}{\partial z} = 0,$$

and we obtain the following relationship by conducting the time derivative of the above equation,

$$\begin{aligned} \frac{\partial}{\partial z} \left(\frac{\partial B_z}{\partial t} \right) &= -\nabla_h \cdot \left(\frac{\partial \mathbf{B}_h}{\partial t} \right) \\ &= -\nabla_h \cdot \left(\frac{\partial \mathbf{B}_{h:cf}}{\partial t} \right) \\ &= -\nabla_h \cdot \left\{ -(\nabla \times \mathbf{E}^{(3)})_h \right\} \\ &= -\frac{\partial}{\partial z} (\nabla \times \mathbf{E}^{(3)}) \cdot \mathbf{z}, \end{aligned} \tag{A3}$$

where we used $\nabla \cdot (\nabla \times \mathbf{E}^{(3)}) = 0$. Eq.(A3) can be described by taking into account Eq.(17), as follows,

$$\frac{\left(\frac{\partial B_z^{(3)}}{\partial t} \right)_{z=+\frac{1}{2}\Delta z} - \left(\frac{\partial B_z^{(3)}}{\partial t} \right)_{z=0}}{\frac{1}{2}\Delta z} = -\nabla_h \cdot \left(\frac{\partial \mathbf{B}_{h:cf}}{\partial t} \right).$$

Since $B_z^{(3)}$ should be zero at the photosphere to avoid overlapping with $B_z^{(1)}$,

$$\left(\frac{\partial B_z^{(3)}}{\partial t} \right)_{z=+\frac{1}{2}\Delta z} = -\frac{1}{2}\Delta z \nabla_h \cdot \left(\frac{\partial \mathbf{B}_{h:cf}}{\partial t} \right). \tag{A4}$$

When we make same assumption as when we obtained $\mathbf{E}^{(1)}$,

$$\mathbf{E}^{(3)}|_{z=+\frac{1}{2}\Delta z} = \mathbf{z} \times \nabla_h \Phi^{(3)} = \left(-\frac{\partial \Phi^{(3)}}{\partial y}, \frac{\partial \Phi^{(3)}}{\partial x}, 0 \right), \tag{A5}$$

the equation

$$\mathbf{z} \cdot (\nabla \times \mathbf{E}^{(3)}) = \left(\frac{\partial^2 \Phi^{(3)}}{\partial x^2} + \frac{\partial^2 \Phi^{(3)}}{\partial y^2} \right) = -\frac{\partial B_z^{(3)}}{\partial t}, \tag{A6}$$

is obtained from equation(17). Eventually we can obtain the third poisson equation,

$$\nabla_h^2 \Phi^{(3)} = \frac{1}{2}\Delta z \nabla_h \cdot \left(\frac{\partial \mathbf{B}_{h:cf}}{\partial t} \right).$$

B. Performances of the Poisson Equations

We show the performances of the Poisson equations (14), (15), and (16) by evaluating the following values,

$$\begin{aligned}
 L_1 &= \int \left| \nabla^2 \Phi^{(1)} - \frac{\partial B_z}{\partial t} \right| dV, \\
 L_2 &= \int \left| \nabla^2 \Phi^{(2)} - \mathbf{z} \cdot \left(\nabla \times \frac{\partial \mathbf{B}_{h:df}}{\partial t} \right) \right| dV, \\
 L_3 &= \int \left| \nabla_h^2 \Phi^{(3)} - \frac{1}{2} \Delta z \nabla_h \cdot \left(\frac{\partial \mathbf{B}_{h:cf}}{\partial t} \right) \right| dV,
 \end{aligned} \tag{B1}$$

and

$$\begin{aligned}
 ER_1 &= \left| \nabla^2 \Phi^{(1)} \right|_{max} - \left| \frac{\partial B_z}{\partial t} \right|_{max}, \\
 ER_2 &= \left| \nabla^2 \Phi^{(2)} \right|_{max} - \left| \mathbf{z} \cdot \left(\nabla \times \frac{\partial \mathbf{B}_{h:df}}{\partial t} \right) \right|_{max}, \\
 ER_3 &= \left| \nabla_h^2 \Phi^{(3)} \right|_{max} - \left| \frac{1}{2} \Delta z \nabla_h \cdot \left(\frac{\partial \mathbf{B}_{h:cf}}{\partial t} \right) \right|_{max}.
 \end{aligned} \tag{B2}$$

When the solutions of the each Poisson equation are correctly obtained, these values completely drop to zero. The Poisson equation is solved numerically by a simple Gauss-Seidel method based on the second order finite difference method and the initial Φ is given as zero. Figures A1a and b show the iteration profile of L_n and ER_n , respectively, where $n=1, 2, 3$. We find that the each value dramatically decreases during the each iteration and eventually saturates at a very low value compared to the initial value. Therefore, the solutions would be obtained with good accuracy.

C. Reproducibility of the Photospheric Magnetic Field

We check how much reproducibility of the photospheric magnetic field from the electric field through the equations (20) has. Following Hayashi et al. (2018), the bottom magnetic field should be reproduced perfectly through the data-driven simulation but it depends on the accuracy of the Poisson solver. Following them, we also make scatter plots for the photospheric magnetic field of the ground-truth data vs. the magnetic field reproduced via the data-driven simulation using the electric fields. Figure A2 shows the scatter plots for B_x and B_y in the twisting phase from $t=0 \sim t=11.25$. Note that the B_z component is not plotted because this does not change during this time period. These plots are almost along a function, $y = x$, *i.e.*, the magnetic field is reproduced well from the data-driven simulation.

Figure A3 shows these scatter plots in the erupting phase, which are the same format as in Fig. A2 except B_z is plotted. Although there's a little dispersions compared to previous cases (however the correlation coefficient is over 0.99), the scatter plots are mostly along a line of $y = x$. So, throughout the simulation, the boundary magnetic field is reproduced well from the data-driven simulation based on the given electric fields.

REFERENCES

- Amari, T., Luciani, J. F., Mikic, Z., et al. 2000, *ApJ*, 529, L49. doi:10.1086/312444
- Amari, T., Luciani, J. F., Aly, J. J., et al. 2003, *ApJ*, 585, 1073
- Berger, M. A. & Prior, C. 2006, *Journal of Physics A Mathematical General*, 39, 8321. doi:10.1088/0305-4470/39/26/005
- Bobra, M. G., Sun, X., Hoeksema, J. T., et al. 2014, *Sol. Phys.*, 289, 3549. doi:10.1007/s11207-014-0529-3
- Cheung, M. C. M. & DeRosa, M. L. 2012, *ApJ*, 757, 147. doi:10.1088/0004-637X/757/2/147
- Clyne, J., & Rast, M. 2005, *Proc. SPIE*, 284
- Clyne, J., Mininni, P., Norton, A., et al. 2007, *New Journal of Physics*, 9, 301
- Dedner, A., Kemm, F., Kröner, D., et al. 2002, *Journal of Computational Physics*, 175, 645
- Fisher, G. H., Welsch, B. T., Abbett, W. P., et al. 2010, *ApJ*, 715, 242. doi:10.1088/0004-637X/715/1/242
- Fisher, G. H., Kazachenko, M. D., Welsch, B. T., et al. 2020, *ApJS*, 248, 2. doi:10.3847/1538-4365/ab8303
- Guo, Y., Xia, C., Keppens, R., et al. 2019, *ApJ*, 870, L21. doi:10.3847/2041-8213/aafabf
- Goode, P. R. & Cao, W. 2012, *Proc. SPIE*, 8444, 844403. doi:10.1117/12.925494
- Hayashi, K., Feng, X., Xiong, M., et al. 2018, *ApJ*, 855, 11
- Hayashi, K., Feng, X., Xiong, M., et al. 2019, *ApJ*, 871, L28
- Inoue, S., Kusano, K., Magara, T., et al. 2011, *ApJ*, 738, 161. doi:10.1088/0004-637X/738/2/161

- Inoue, S., Hayashi, K., Magara, T., et al. 2014, *ApJ*, 788, 182. doi:10.1088/0004-637X/788/2/182
- Inoue, S. 2016, *Progress in Earth and Planetary Science*, 3, 19. doi:10.1186/s40645-016-0084-7
- Inoue, S., Kusano, K., Büchner, J., et al. 2018, *Nature Communications*, 9, 174. doi:10.1038/s41467-017-02616-8
- Inoue, S., Magara, T., Watari, S., et al. 2012, *ApJ*, 747, 65. doi:10.1088/0004-637X/747/1/65
- Jiang, C., Wu, S. T., Feng, X., et al. 2014, *ApJ*, 780, 55. doi:10.1088/0004-637X/780/1/55
- Jiang, C., Wu, S. T., Feng, X., et al. 2016, *Nature Communications*, 7, 11522. doi:10.1038/ncomms11522
- Jiang, C., Yan, X., Feng, X., et al. 2017, *ApJ*, 850, 8. doi:10.3847/1538-4357/aa917a
- Jiang, C., Feng, X., & Hu, Q. 2018, *ApJ*, 866, 96. doi:10.3847/1538-4357/aadd08
- Jiang, C., Bian, X., Sun, T., et al. 2021, *Frontiers in Physics*, 9, 224. doi:10.3389/fphy.2021.646750
- Jiang, C., Feng, X., Guo, Y., et al. 2022, *The Innovation*, 3, 100236. doi:10.1016/j.xinn.2022.100236
- Kaneko, T., Park, S.-H., & Kusano, K. 2021, *ApJ*, 909, 155. doi:10.3847/1538-4357/abe414
- Kawabata, Y., Asensio Ramos, A., Inoue, S., et al. 2020, *ApJ*, 898, 32. doi:10.3847/1538-4357/ab9816
- Kawabata, Y., Inoue, S., & Shimizu, T. 2020, *ApJ*, 895, 105. doi:10.3847/1538-4357/ab8ea9
- Kawabata, Y., Iida, Y., Doi, T., et al. 2018, *ApJ*, 869, 99. doi:10.3847/1538-4357/aaebfc
- Kazachenko, M. D., Fisher, G. H., & Welsch, B. T. 2014, *ApJ*, 795, 17. doi:10.1088/0004-637X/795/1/17
- Kang, J., Inoue, S., Kusano, K., et al. 2019, *ApJ*, 887, 263. doi:10.3847/1538-4357/ab5582
- Leake, J. E., Linton, M. G., & Schuck, P. W. 2017, *ApJ*, 838, 113. doi:10.3847/1538-4357/aa6578
- Liu, C., Chen, T., & Zhao, X. 2019, *A&A*, 626, A91. doi:10.1051/0004-6361/201935225

- Lumme, E., Pomoell, J., & Kilpua, E. K. J. 2017, *Sol. Phys.*, 292, 191. doi:10.1007/s11207-017-1214-0
- Metcalf, T. R., Jiao, L., McClymont, A. N., et al. 1995, *ApJ*, 439, 474. doi:10.1086/175188
- Muhamad, J., Kusano, K., Inoue, S., et al. 2017, *ApJ*, 842, 86. doi:10.3847/1538-4357/aa750e
- Muhamad, J., Kusano, K., Inoue, S., et al. 2018, *ApJ*, 863, 162. doi:10.3847/1538-4357/aad181
- Nayak, S. S., Bhattacharyya, R., & Kumar, S. 2021, *Physics of Plasmas*, 28, 024502. doi:10.1063/5.0035086
- Pesnell, W. D., Thompson, B. J., & Chamberlin, P. C. 2012, *Sol. Phys.*, 275, 3. doi:10.1007/s11207-011-9841-3
- Pomoell, J., Lumme, E., & Kilpua, E. 2019, *Sol. Phys.*, 294, 41. doi:10.1007/s11207-019-1430-x
- Prasad, A., Dissauer, K., Hu, Q., et al. 2020, *ApJ*, 903, 129. doi:10.3847/1538-4357/abb8d2
- Price, D. J., Pomoell, J., & Kilpua, E. K. J. 2020, *A&A*, 644, A28. doi:10.1051/0004-6361/202038925
- Rast, M. P., Bello González, N., Bellot Rubio, L., et al. 2021, *Sol. Phys.*, 296, 70. doi:10.1007/s11207-021-01789-2
- Sakurai, T. 1982, *Sol. Phys.*, 76, 301
- Savcheva, A., Pariat, E., van Ballegoijen, A., et al. 2012, *ApJ*, 750, 15. doi:10.1088/0004-637X/750/1/15
- Shibata, K. & Magara, T. 2011, *Living Reviews in Solar Physics*, 8, 6. doi:10.12942/lrsp-2011-6
- Schrijver, C. J., DeRosa, M. L., Metcalf, T., et al. 2008, *ApJ*, 675, 1637. doi:10.1086/527413
- Schuck, P. W. 2008, *ApJ*, 683, 1134. doi:10.1086/589434
- Sun, X., Hoeksema, J. T., Liu, Y., et al. 2012, *ApJ*, 748, 77. doi:10.1088/0004-637X/748/2/77
- Toriumi, S. & Wang, H. 2019, *Living Reviews in Solar Physics*, 16, 3. doi:10.1007/s41116-019-0019-7
- Toriumi, S., Takasao, S., Cheung, M. C. M., et al. 2020, *ApJ*, 890, 103

Wang, H., Liu, C., Ahn, K., et al. 2017, *Nature Astronomy*, 1, 0085. doi:10.1038/s41550-017-0085

Welsch, B. T., Abbett, W. P., De Rosa, M. L., et al. 2007, *ApJ*, 670, 1434. doi:10.1086/522422

Woods, M. M., Inoue, S., Harra, L. K., et al. 2020, *ApJ*, 890, 84. doi:10.3847/1538-4357/ab6bc8

Xia, C., Keppens, R., & Guo, Y. 2014, *ApJ*, 780, 130. doi:10.1088/0004-637X/780/2/130

Yamasaki, D., Inoue, S., Nagata, S., et al. 2021, *ApJ*, 908, 132. doi:10.3847/1538-4357/abcfbb

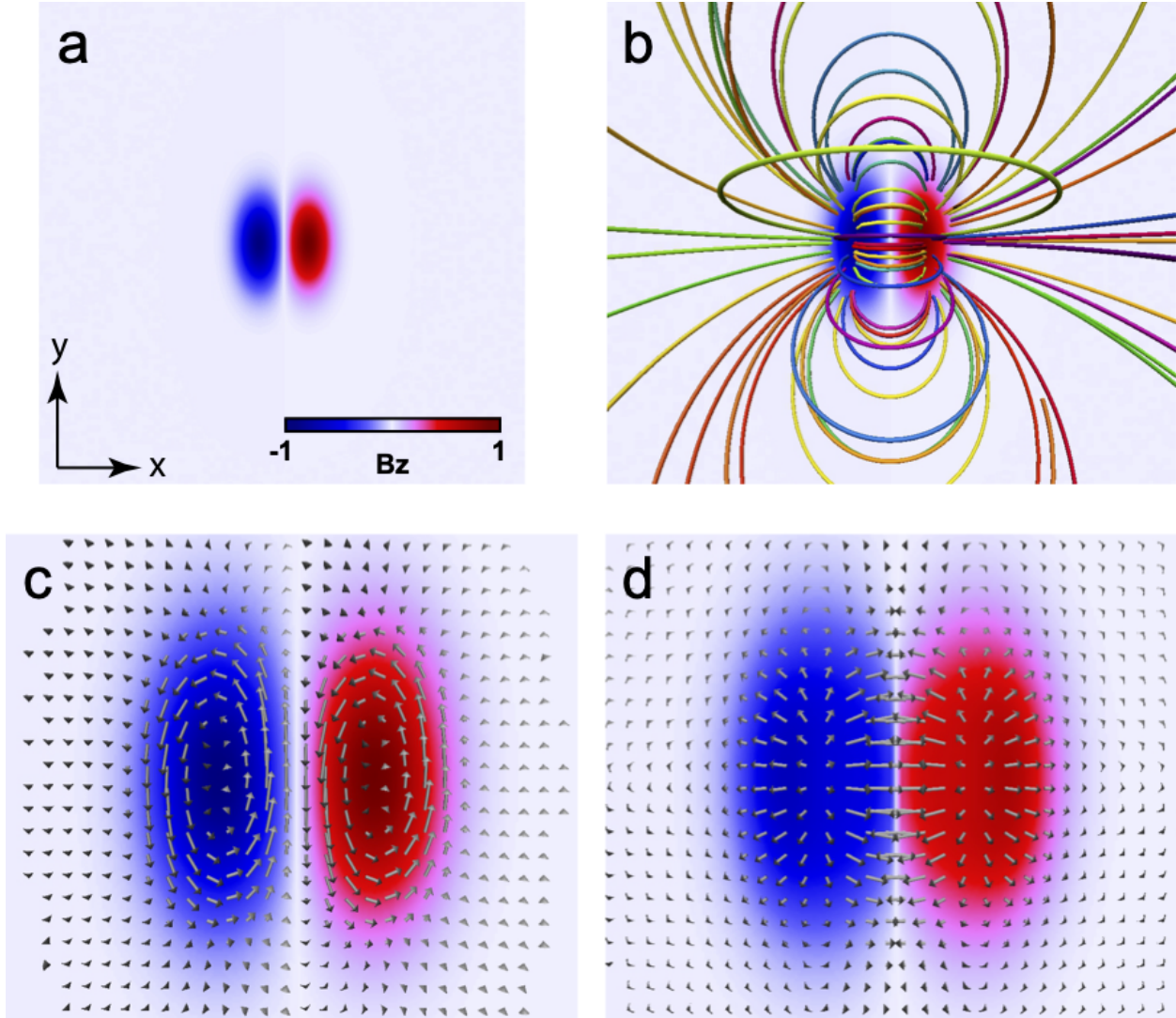


Fig. 1.— **a** A bipolar magnetic field given at the bottom surface where the red and blue correspond to the positive and negative polarities, respectively. The full simulation region is plotted in X- and Y- directions. **b** The potential magnetic field which is extrapolated from the bipolar magnetic field is shown in **a**. This is used as the initial condition of the MHD simulation. **c** Twisting motion of the velocity given on the bipolar field, which can keep the distribution of the bipolar field. **d** Diverging motion of the velocity given on the bipolar field. This velocity plays a role as converging motion at the PIL.

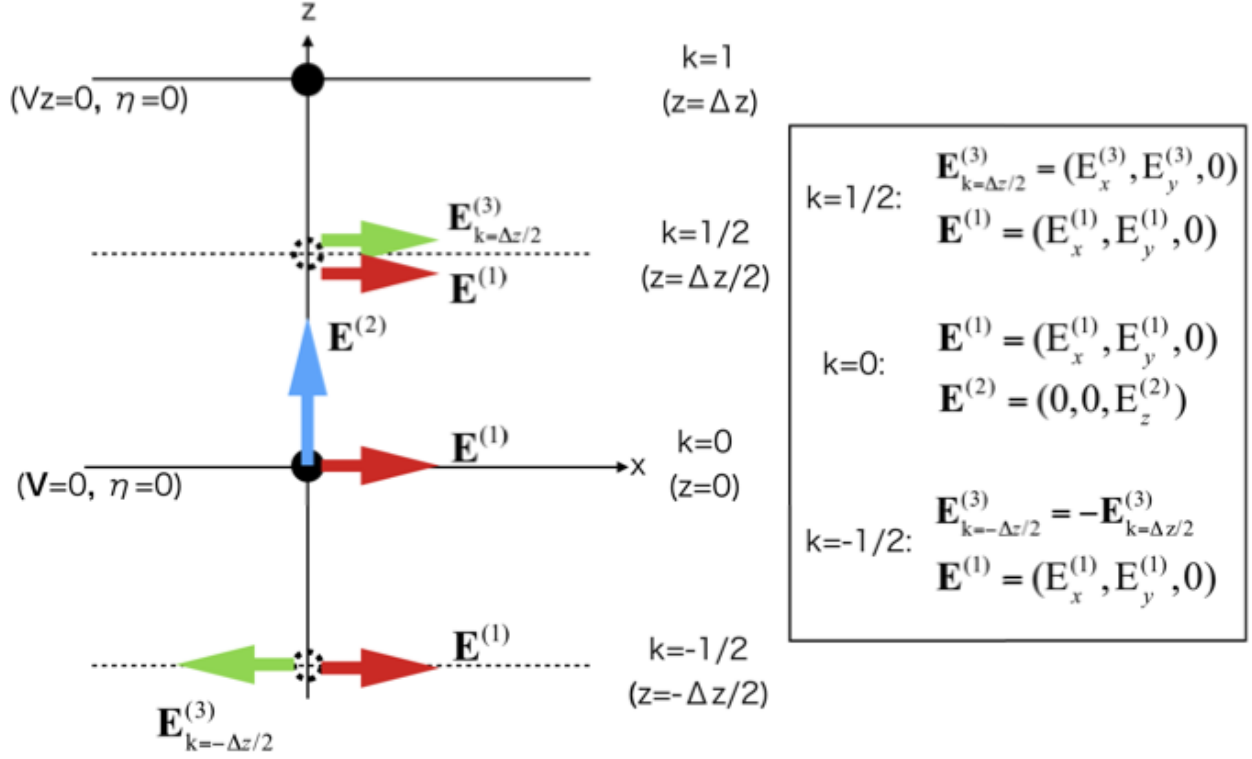


Fig. 2.— The positions of each electric field, $\mathbf{E}^{(1)}$, $\mathbf{E}^{(2)}$ and $\mathbf{E}^{(3)}$ that drive the coronal magnetic field, proposed by Hayashi et al. (2018). $z=0$ corresponds to the bottom boundary (photosphere) and $z=\Delta z$ corresponds to a location one grid above the bottom surface where Δz is a distance between neighboring grids set in this study. All physical values are defined at the black circles in this simulation where k takes integer value. $\mathbf{E}^{(1)}$ and $\mathbf{E}^{(3)}$ are given at $k=\pm 1/2$. The right square summarizes the electric fields which are given at $k=1$ and $k=\pm 1/2$.

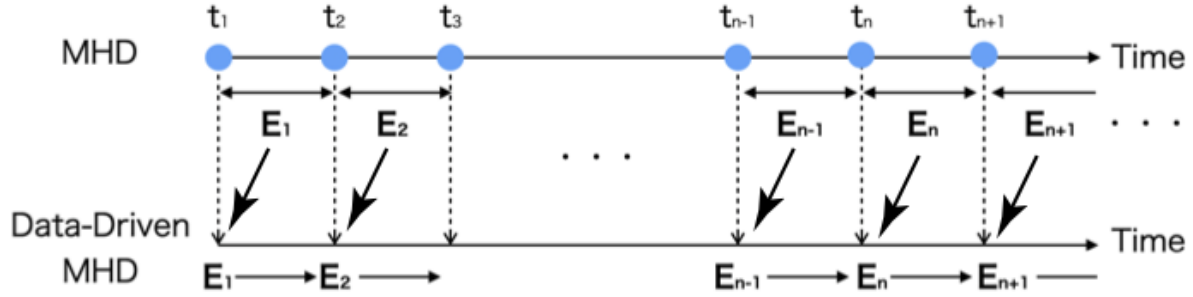


Fig. 3.— This cartoon shows how advances in time are handled by the data-driven MHD simulation. The blue circle corresponds to the ground-truth data. We calculate the electric field E_n at the bottom surface from the magnetic fields B_n and B_{n+1} at $t = n$ and $t = n + 1$ in the ground-truth data where $n = 1, 2, 3, \dots$. In the data-driven simulation, E_n drives an entire magnetic field in a time range from t_n to t_{n+1} . In this study, the time interval $t_{n+1} - t_n$ is set to 0.5625.

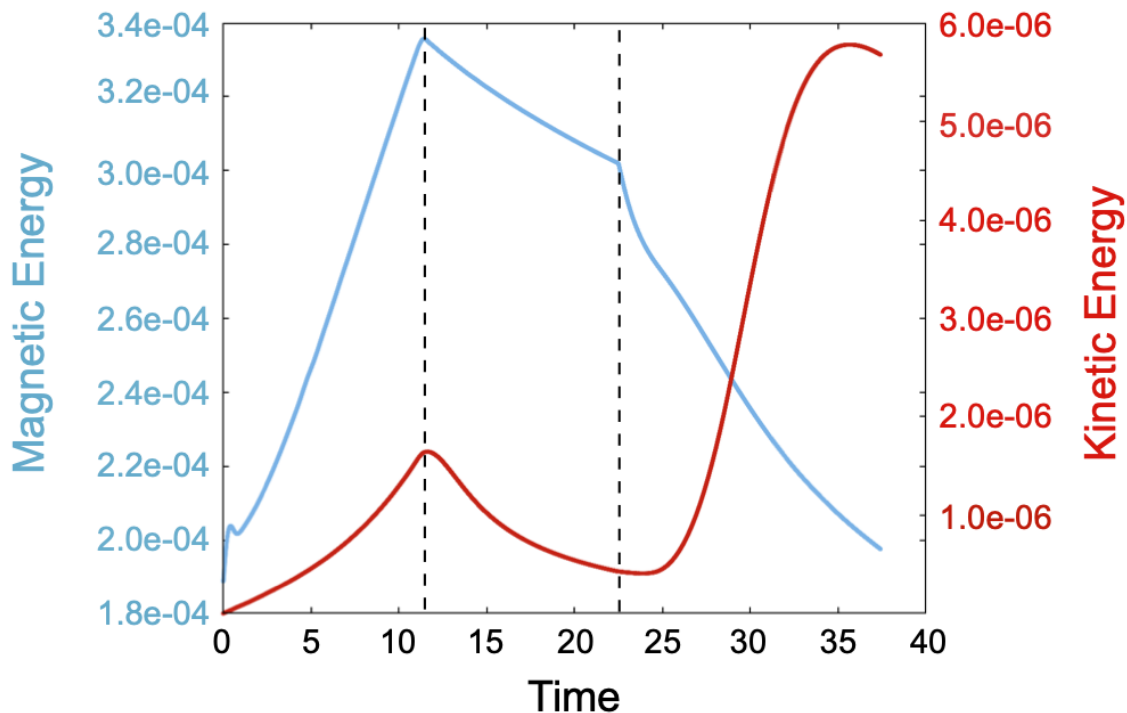


Fig. 4.— Temporal evolutions of the magnetic energy and the kinetic energy are plotted in blue and red, respectively. These are driven by the twisting and diverging motions on the photosphere given in the MHD simulation. The vertical dashed lines are set at $t \sim 11.25$ and $t \sim 22.5$, respectively. The twisting motion as shown in Fig.1c is imposed during a period, $0 \leq t \leq 11.25$ and after that the magnetic field is relaxed, *i.e.*, no external velocity is imposed by $t \sim 22.5$. After $t \sim 22.5$, the converging motion is added on the bottom surface as shown in Fig. 1d.

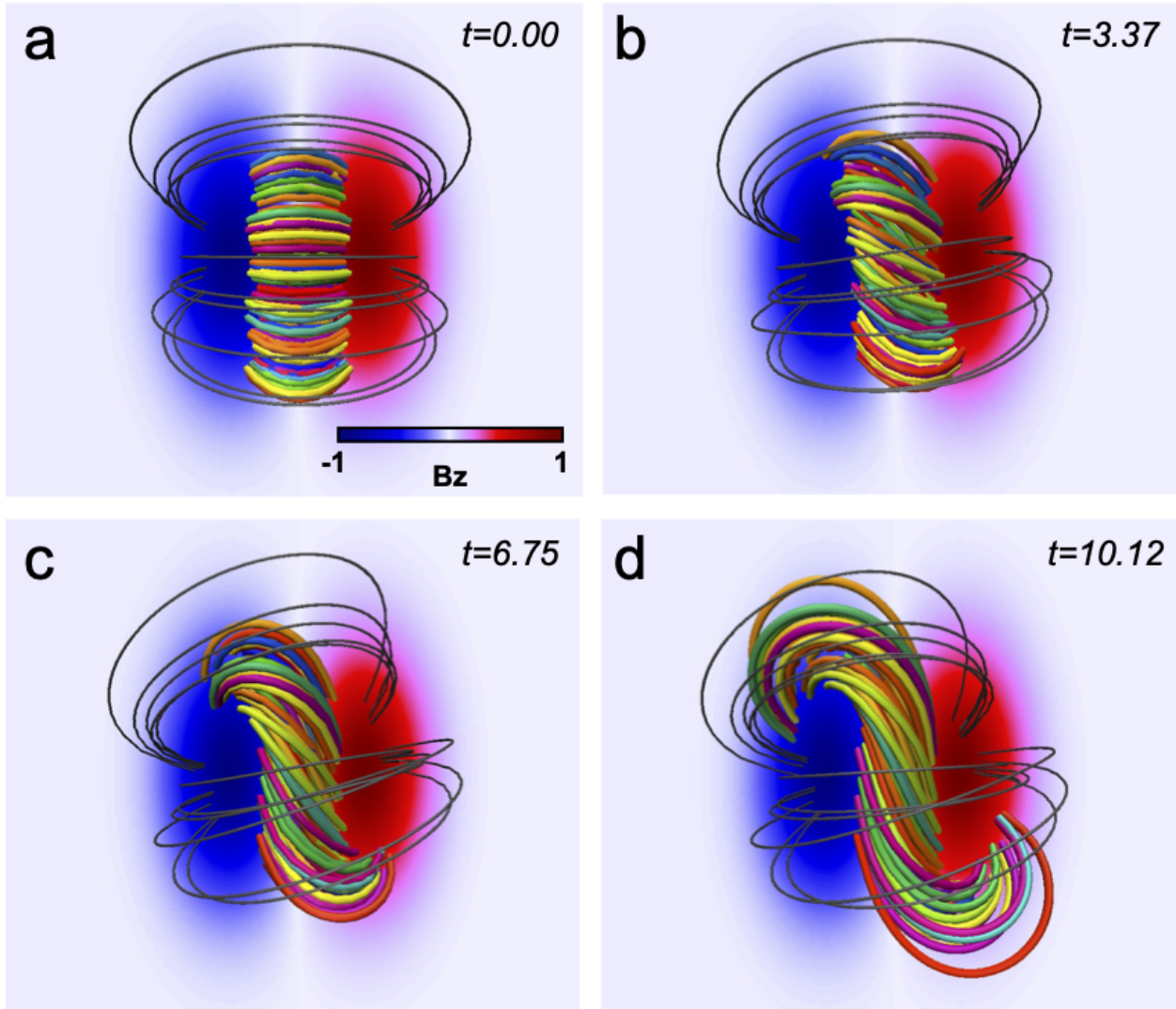


Fig. 5.— **a-b** Temporal evolution of the 3D magnetic field lines associated with the twisting motion imposed on the bipolar field given at the bottom surface. The lines correspond to the magnetic field lines: colored lines are twisted and the black lines are overlying field lines. As time passes, an S-shaped structure is being gradually formed.

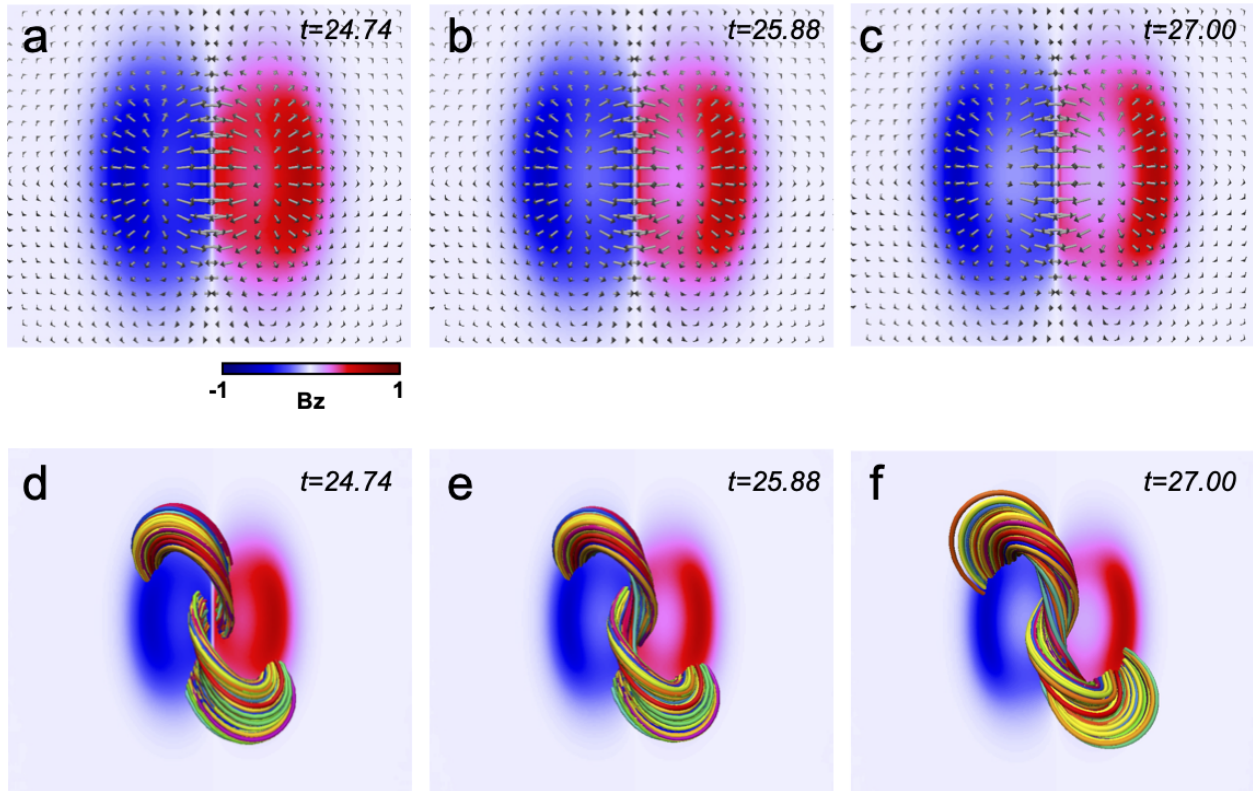


Fig. 6.— **a-c** Temporal evolution of the converging motion given on the bipolar fields and B_z component in color. **d-f** Temporal evolution of the magnetic field lines. In this period, the highly twisted lines (MFR) are being formed, which transitions from the pre-erupting stage to the erupting stage.

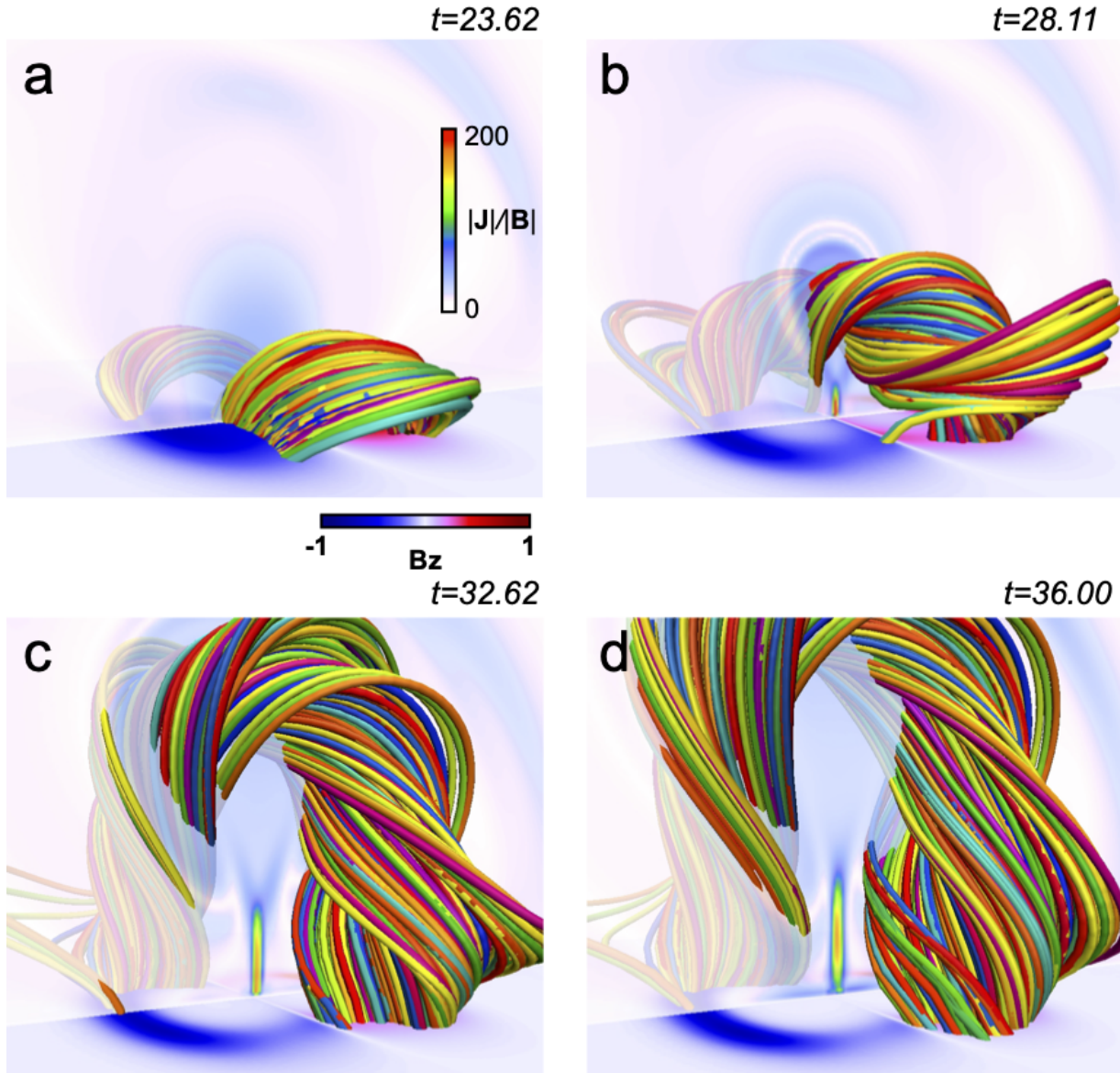


Fig. 7.— **a-d** Temporal evolution of the 3D magnetic field associated with the converging motion imposed on the bipolar field given at the bottom surface. The lines correspond to the magnetic field lines and the value of $|J|/|B|$ is plotted on the vertical cross section. The bottom cross section is plotted in the B_z distribution.

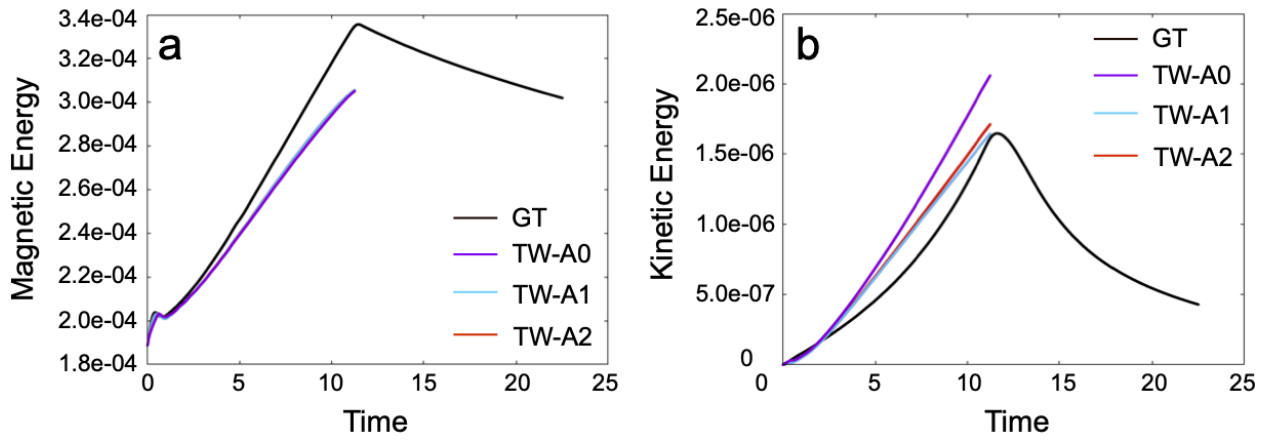


Fig. 8.— **a** Temporal evolution of the magnetic energy in the energy build-up phase where the black, purple, light blue and red, represent the results in the ground-truth data and each case of the data-driven MHD simulation, TW-A0, TW-A1, and TW-A2, respectively. These lines obtained from the data-driven simulations are almost overlapping. **b** Temporal evolution of the kinetic energy. The format is the same as in **a**.

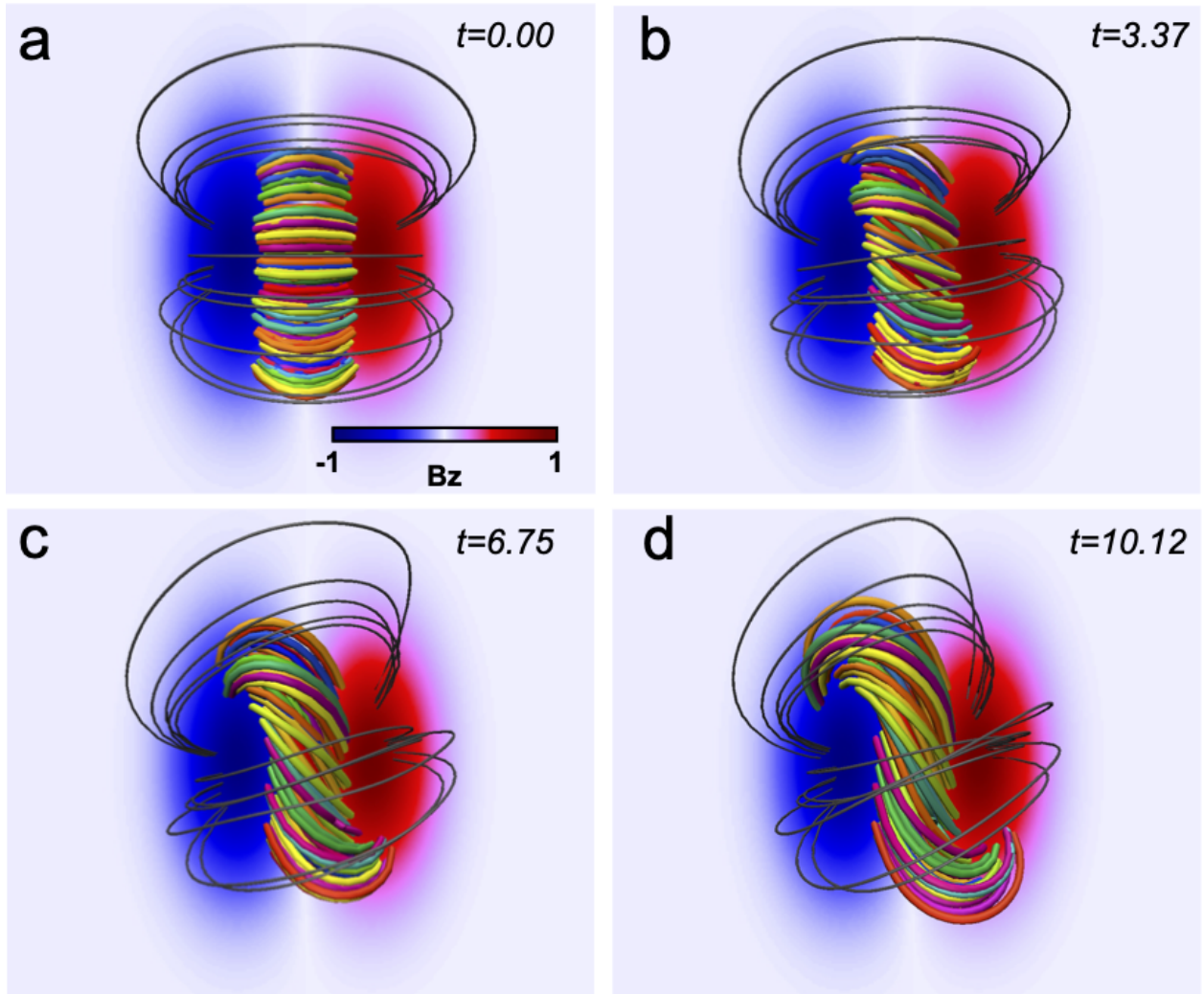


Fig. 9.— **a-d** Temporal evolution of the 3D magnetic field lines obtained from the data-driven MHD simulation (TW-A2). The format of this figure is quite same as the one in Fig.5.

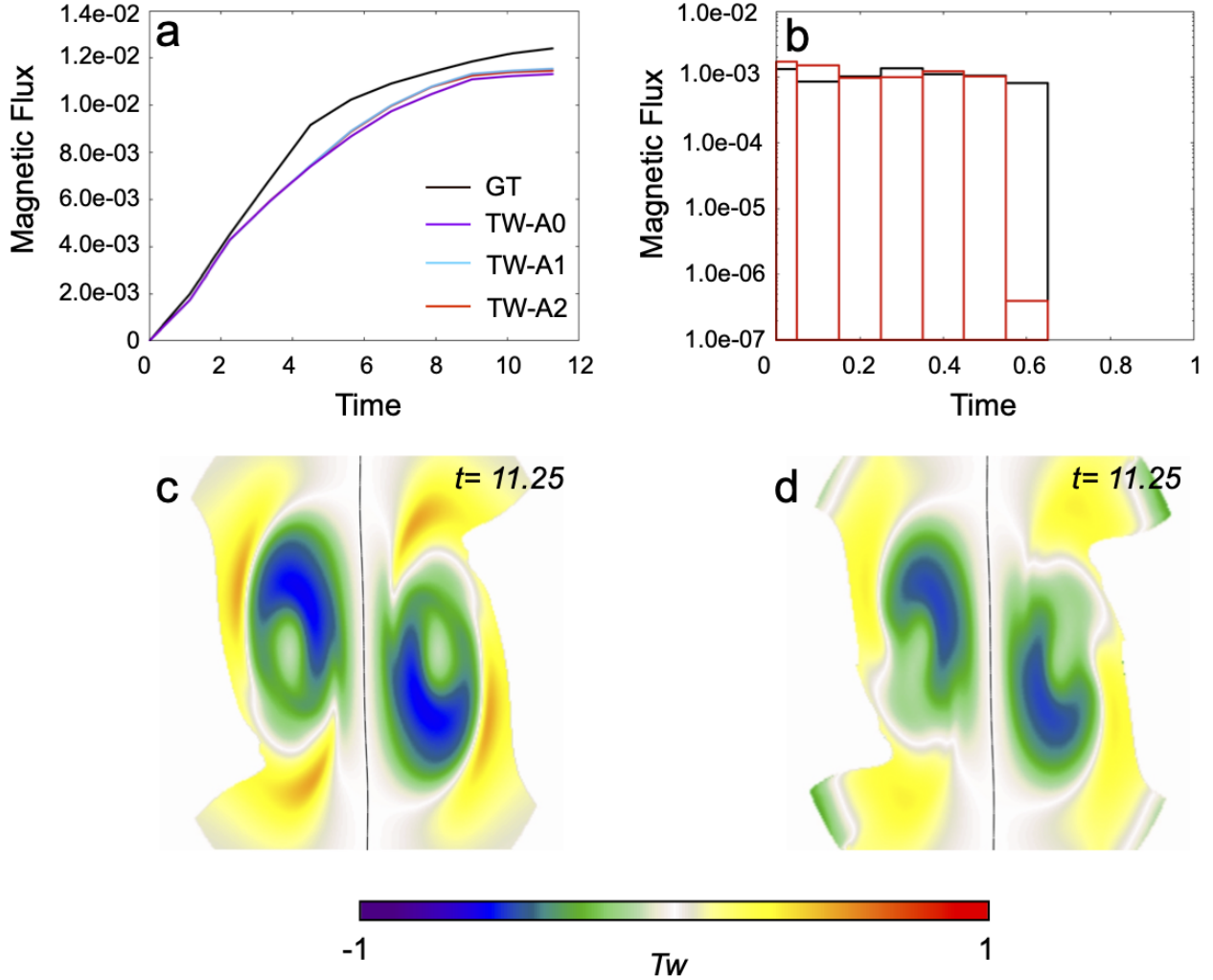


Fig. 10.— **a** Temporal evolution of the magnetic flux dominated by the magnetic field lines which satisfy $T_w \leq -0.1$ where the field lines are traced from the surface one grid above the bottom surface to measure the twist. The each colored line is same format as the ones in Fig.8. **b** Histogram for the magnetic flux vs. T_w from the ground-truth data in black and the data-driven simulation in red (TW-A2), respectively. These results are obtained at $t=11.25$ which is the last time step in the both simulations. **c-d** The snapshots of the twist distribution of each field line, which are mapped on the each bottom surface, at $t=11.25$ in the ground-truth data and in the data-driven MHD simulation (TW-A2). The black line corresponds to the PIL. Strong negative twist regions correspond to the footpoints of the MFR.

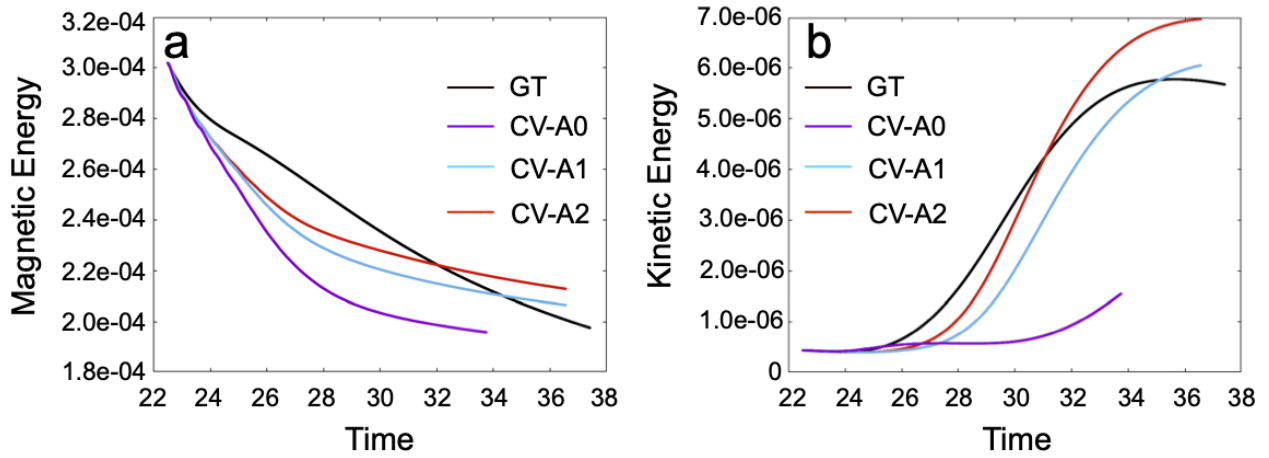


Fig. 11.— **a** Temporal evolution of the magnetic energies in the period from the pre-erupting to the erupting phase. The black, purple, light blue, and red lines are the results obtained from the ground-truth data and the data-driven MHD simulations (CV-A0, CV-A1, and CV-A2), respectively. **b** The temporal evolution of the kinetic energy whose format is the same as in **a**.

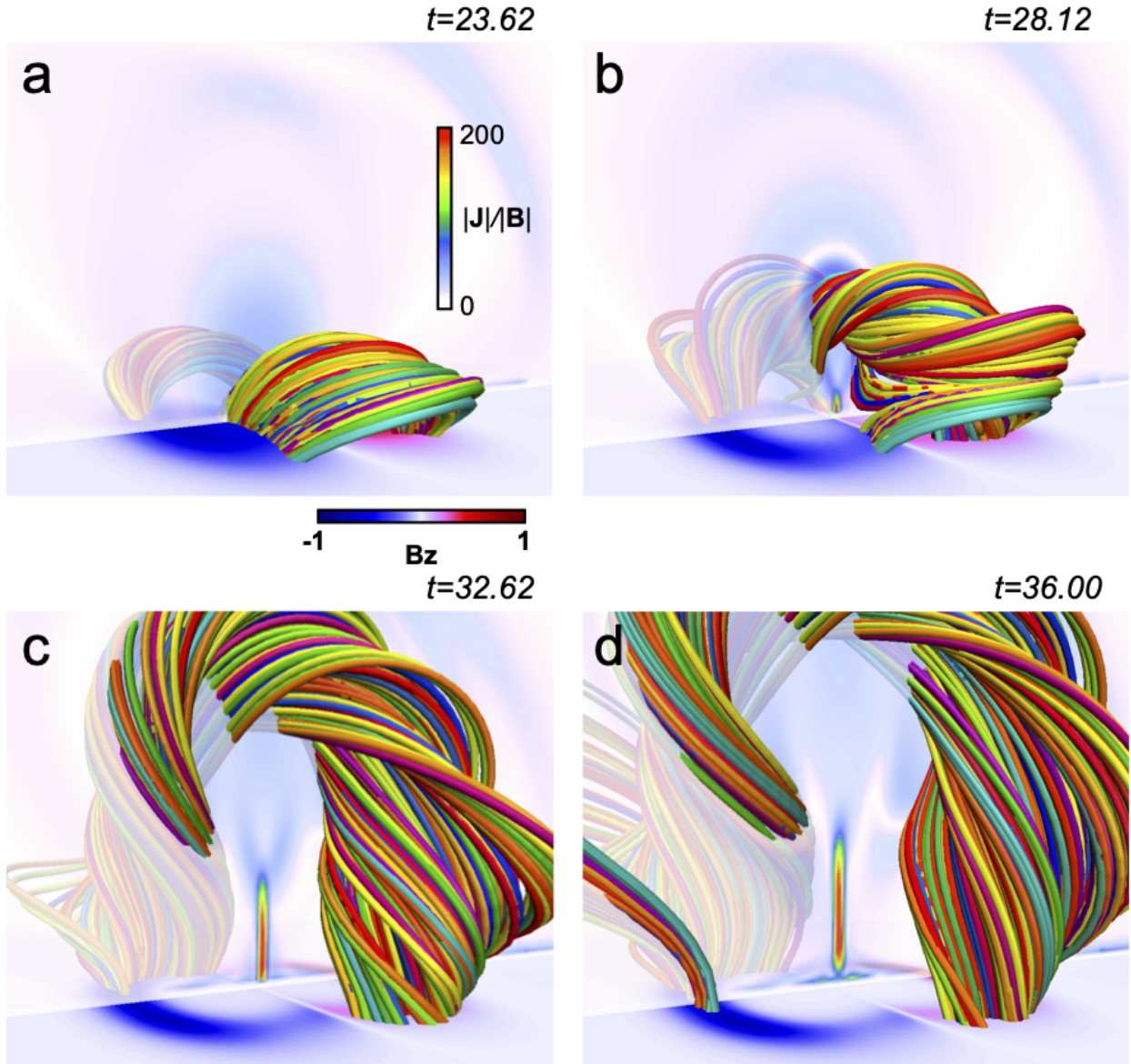


Fig. 12.— **a-d** Temporal evolution of the 3D magnetic field obtained from the data-driven MHD simulation (CV-A2). These formats are the same as those in Fig.7.

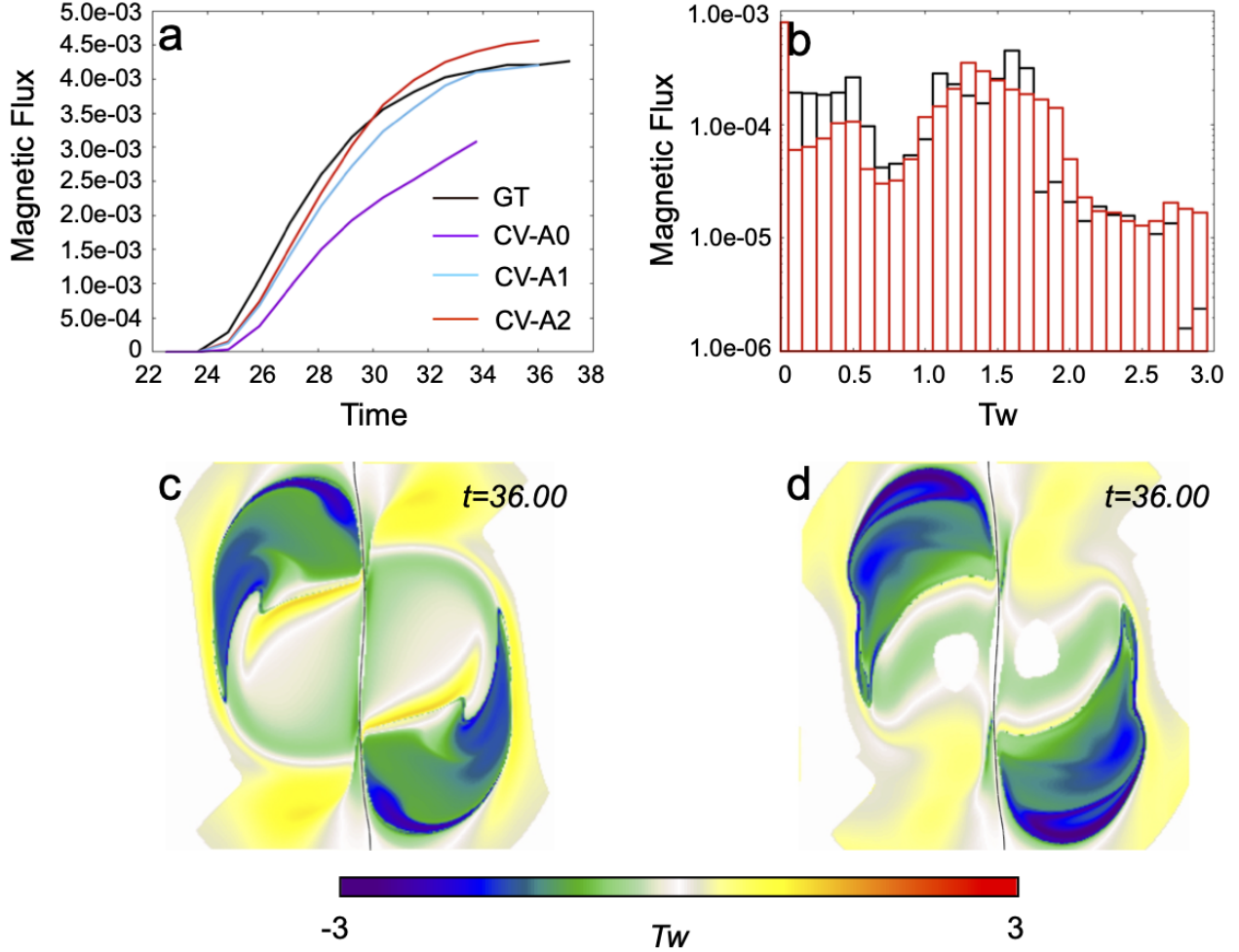


Fig. 13.— **a** Temporal evolution of the magnetic flux dominated by the highly twisted field lines which satisfy $T_w \leq -1.0$. These highly twisted field lines are newly created during the eruption. Each colored line represents the same format as in Fig.11(a). **b** Histogram for the magnetic flux vs. T_w where the black and red lines represent the results obtained from the ground-truth data and the data-driven simulation (CV-A2) at $t=36.00$, respectively. These are results at the last time of the each simulation. **c-d** Snapshots of the twist distribution of each field line, which are mapped on the each surface, obtained from the ground-truth data and the data-driven simulation (CV-A2) at $t=36.00$, respectively. The format is the same as in Figs.10c and d.

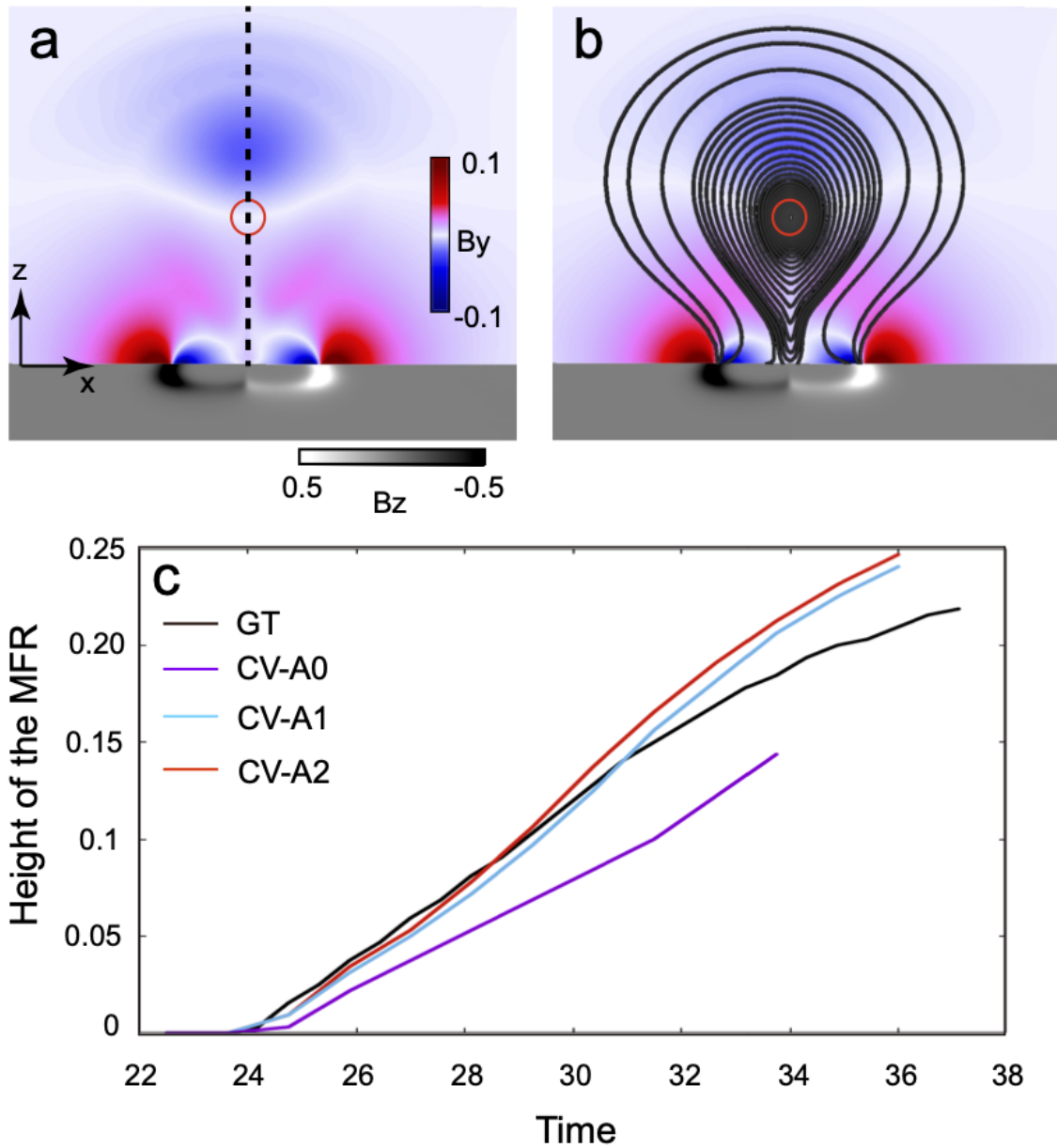


Fig. 14.— **a** The B_x distribution obtained in the ground-truth data is plotted on the vertical cross section at $y = 0.5$ at $t=34.87$. The vertical dashed line is plotted from the position $(x, y)=(0.5, 0.5)$ and the red circle is located at $B_x=0$. **b** The field lines, which are traced in $x - z$ plane, are plotted over (a). The red circle, which is the same one in **a**, points out the center of the MFR. **c** The temporal evolutions of height profile of each MFR calculated from the ground-truth and the each data-driven simulation. The color is the same format as in Fig.11 or Fig.13a.

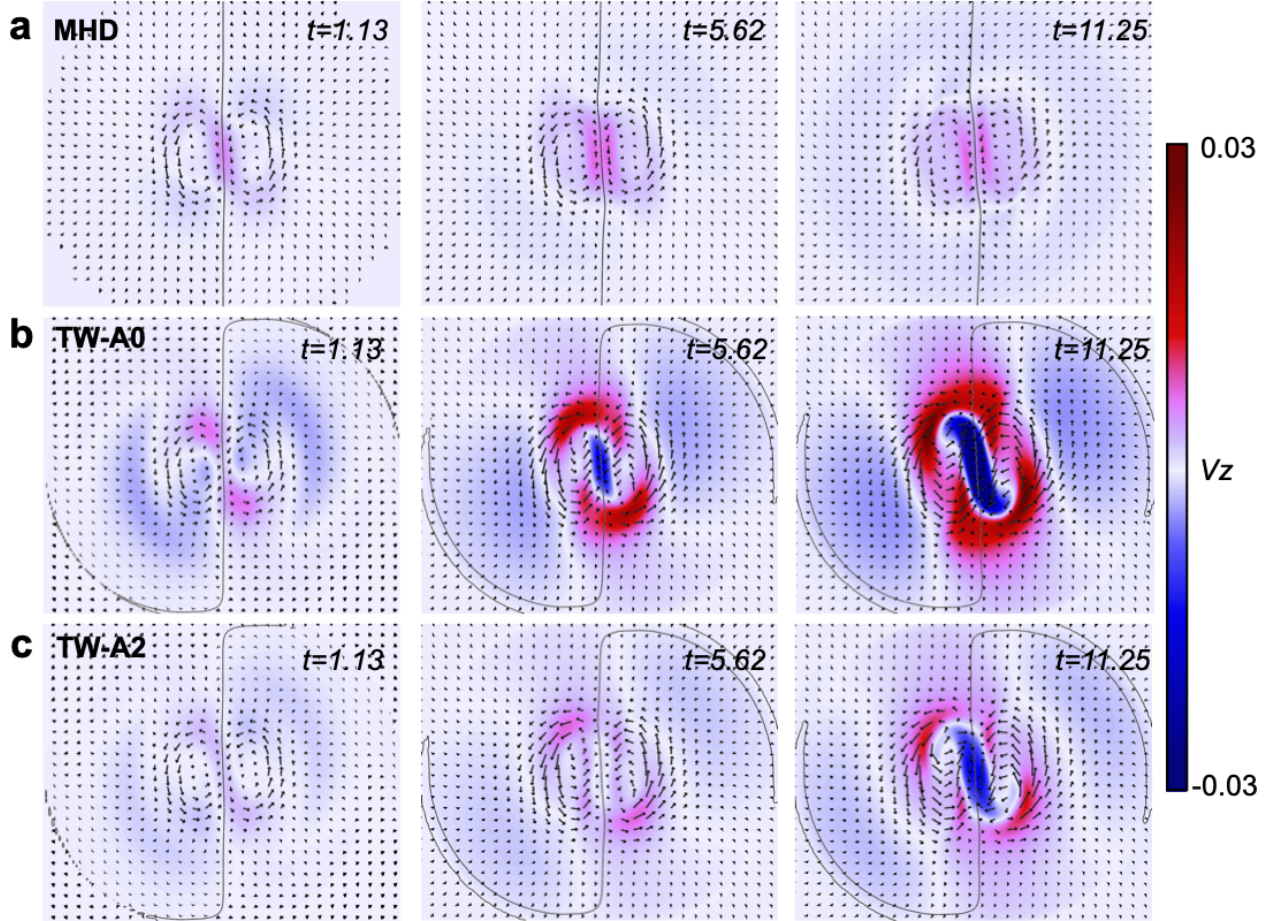


Fig. 15.— Temporal evolutions of the velocity at a surface at $z = 3\Delta$ obtained from the MHD simulation and the results of the data-driven MHD simulations in the cases of TW-A0, and TW-A2. The color shows the v_z distribution while the arrow indicates horizontal velocity $\mathbf{v}_h = (v_x, v_y)$ and the black line corresponds to the PIL.

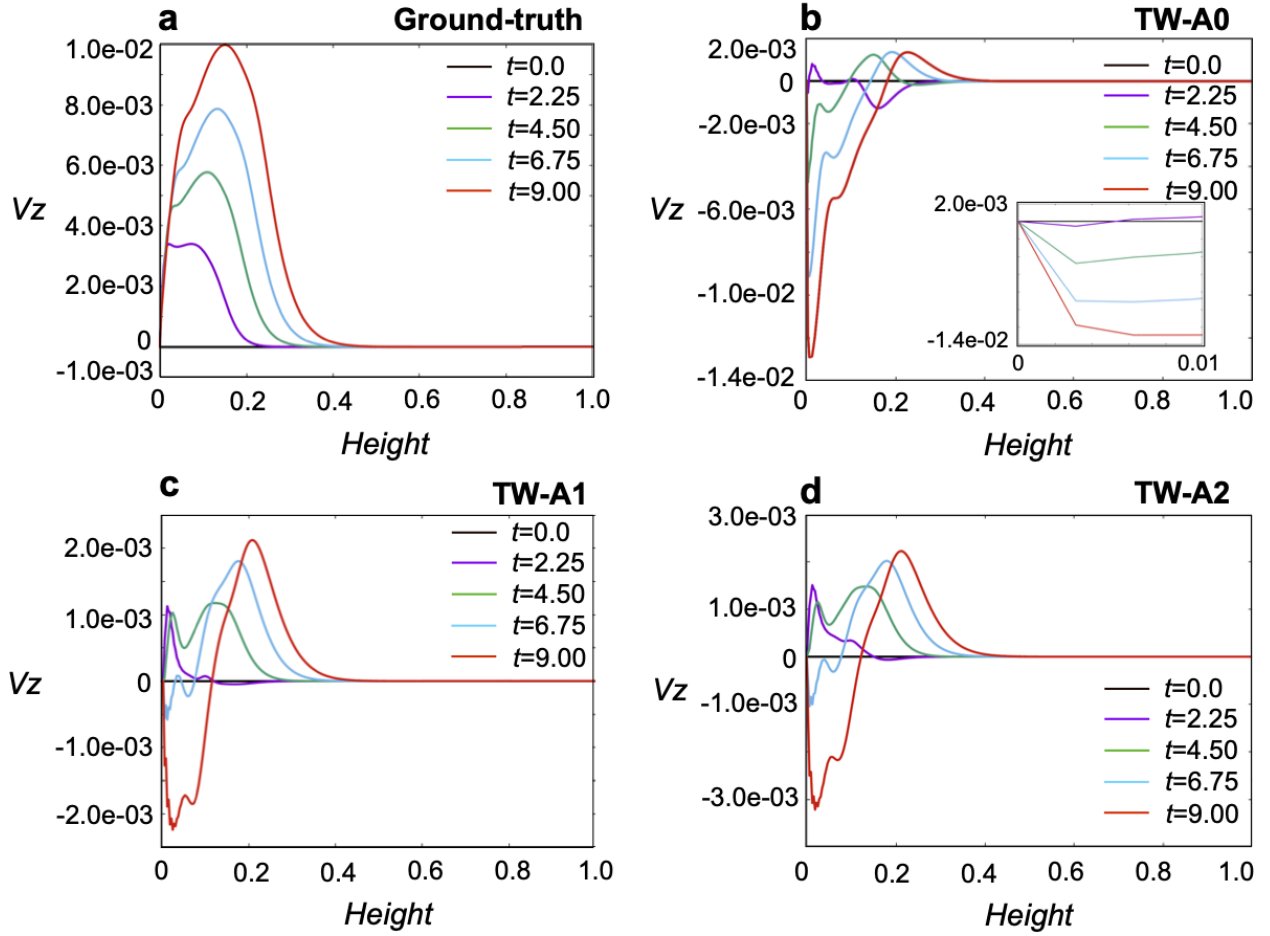


Fig. 16.— The temporal evolution of the v_z at a center of the numerical box which corresponds to $\mathbf{r}_c = (0.5, 0.5, z)$. The vertical and horizontal axes correspond to v_z and height (z), respectively. These velocities are associated with the twisting motion given on the photosphere. **a-d** correspond to the results obtained from the ground-truth data and the data-driven simulations (TW-A0, TW-A1, and TW-A2). The each colored line represents the velocity profile in z -direction at each time where the black, purple, green, blue, and red lines correspond to each time, $t = 0.0, 2.25, 4.50, 6.75, \text{ and } 9.00$, respectively. The small inset corresponds to the enlarged view in the height range from 0 to 0.01.

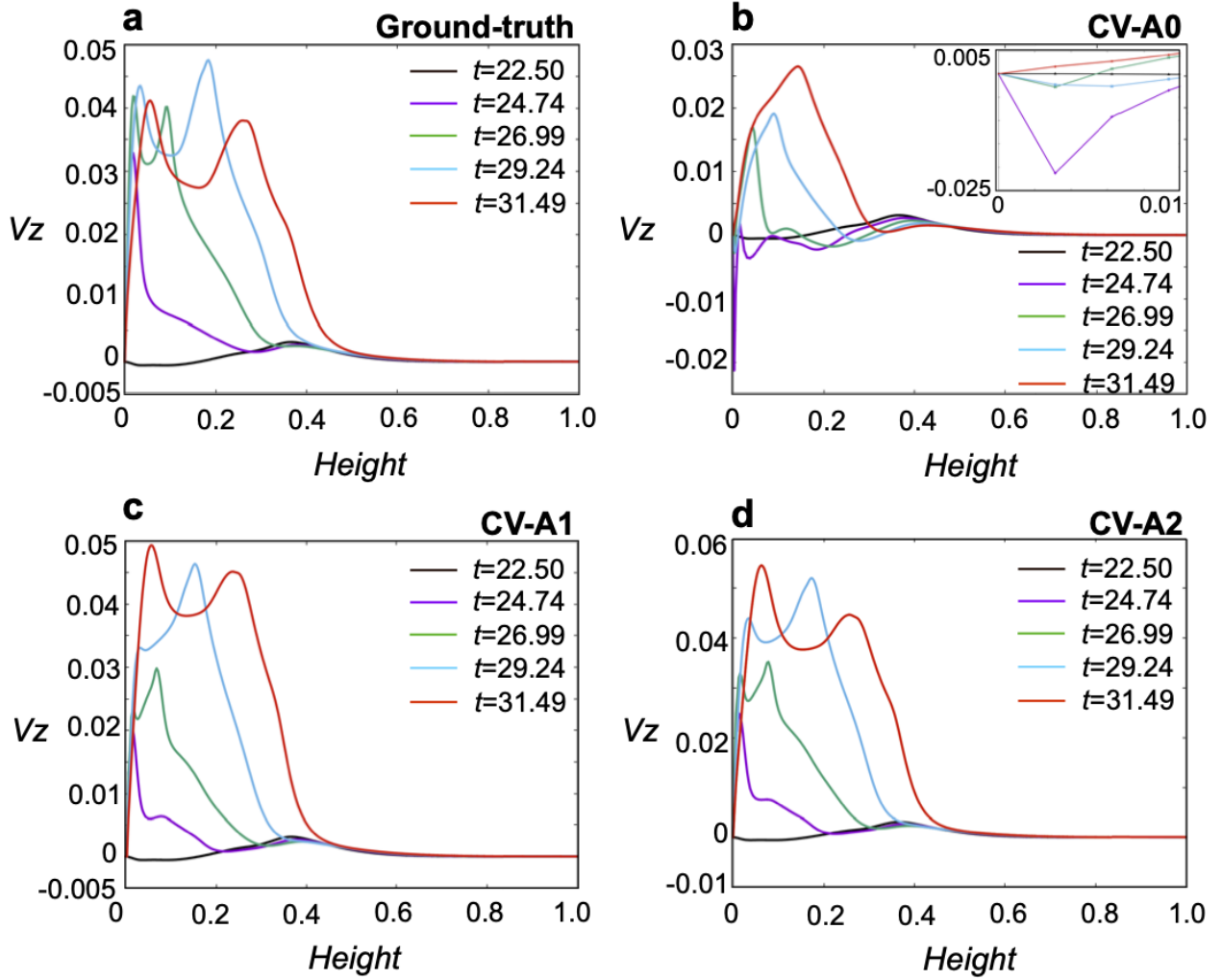


Fig. 17.— The temporal evolution of v_z at a center of the numerical box, associated with the converging motion given on the photosphere. The format is the same as Fig.16 where **a-d** correspond to the results obtained from the ground-truth data and the data-driven MHD simulations (CV-A0, CV-A1, and CV-A2). The black, purple, green, blue, and red lines represent the height profiles of the vertical velocities at $t=22.50$, 24.74, 26.99, 29.24, and 31.49, respectively. The small inset corresponds to the enlarged view in the height range from 0 to 0.01.

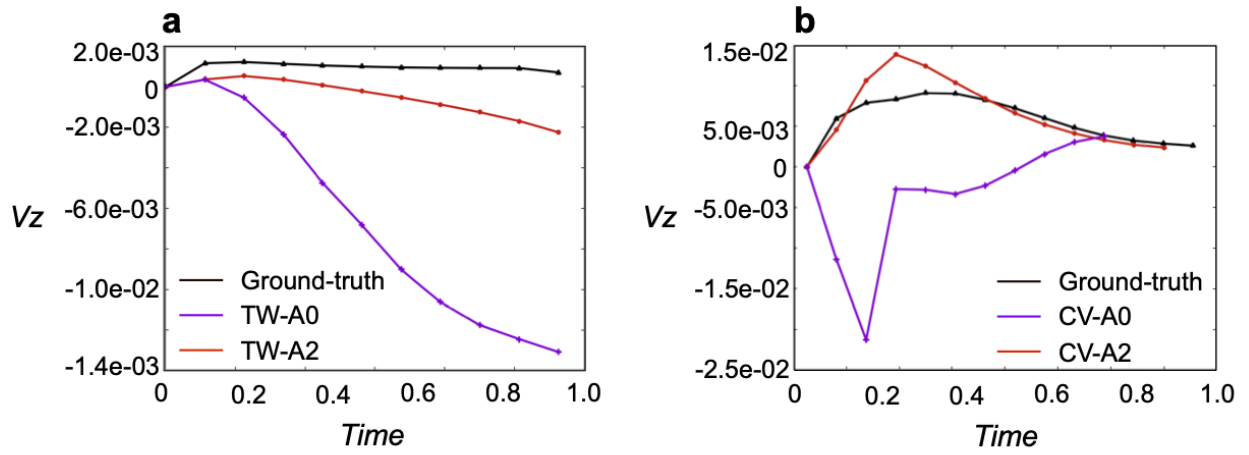


Fig. 18.— **a** Temporal evolution of v_z at $k=1$ is plotted for the each case in the energy buildup stage. Each color, black, purple and red, represents the results obtained from the ground-truth data and the data-driven simulations (TW-A0, and TW A2), respectively. **b** Temporal evolution v_z at $k=1$ is plotted for each case in the energy release stage. Each color, black, purple and red, represents the results obtained from the ground-truth data and the data-driven simulations (CV-A0 and CV-A2), respectively.

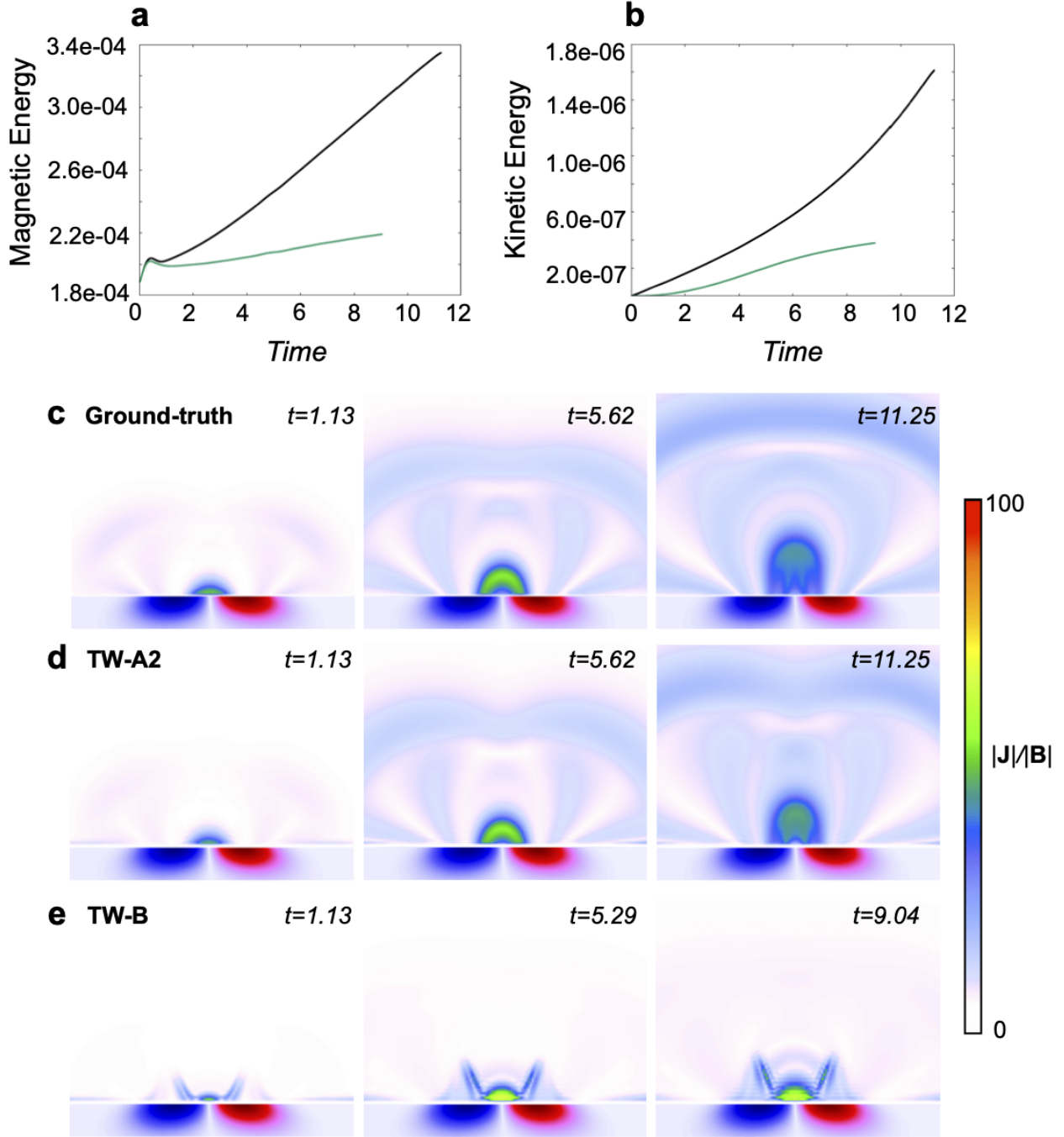


Fig. 19.— **a** The temporal evolution of the magnetic energies obtained from the ground-truth data in black and the data-driven simulation (TW-B) in green. **b** The temporal evolution of the kinetic energies in each case which are in the same format as **a**. **c-e** The temporal evolution of $|\mathbf{J}|/|\mathbf{B}|$ obtained from the ground-truth data and the data-driven simulations (TW-A2, and TW-B), respectively.

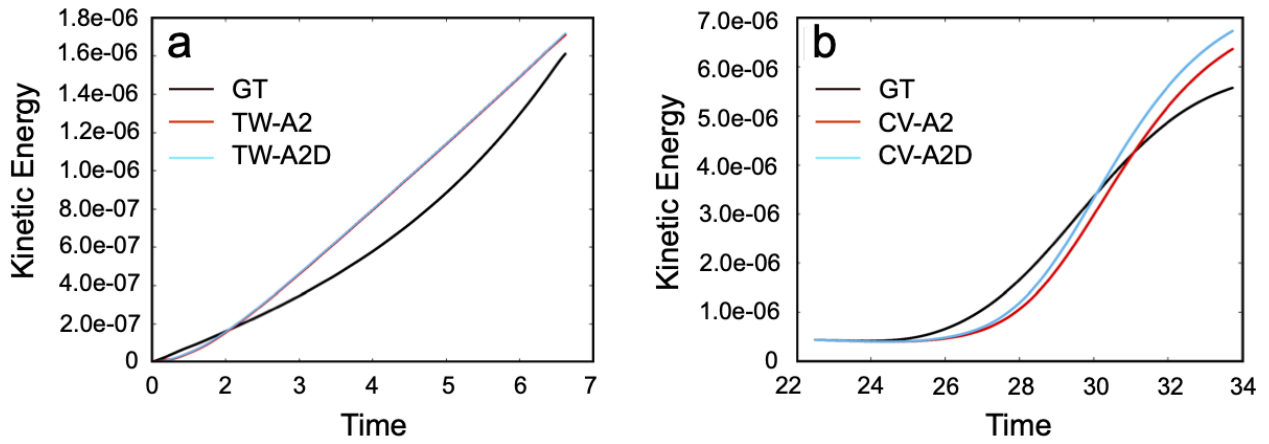


Fig. 20.— **a** The temporal evolutions of the kinetic energy in the twisting phase for the ground-truth data in black, the data-driven simulations (TW-A2 and TW-A2D) shown in red and blue, respectively. TW-A2D has 2.5 times the temporal resolution of TW-A2. **b** The temporal evolutions of the kinetic energy in erupting phase for each case. The format is the same as those shown in **a**.

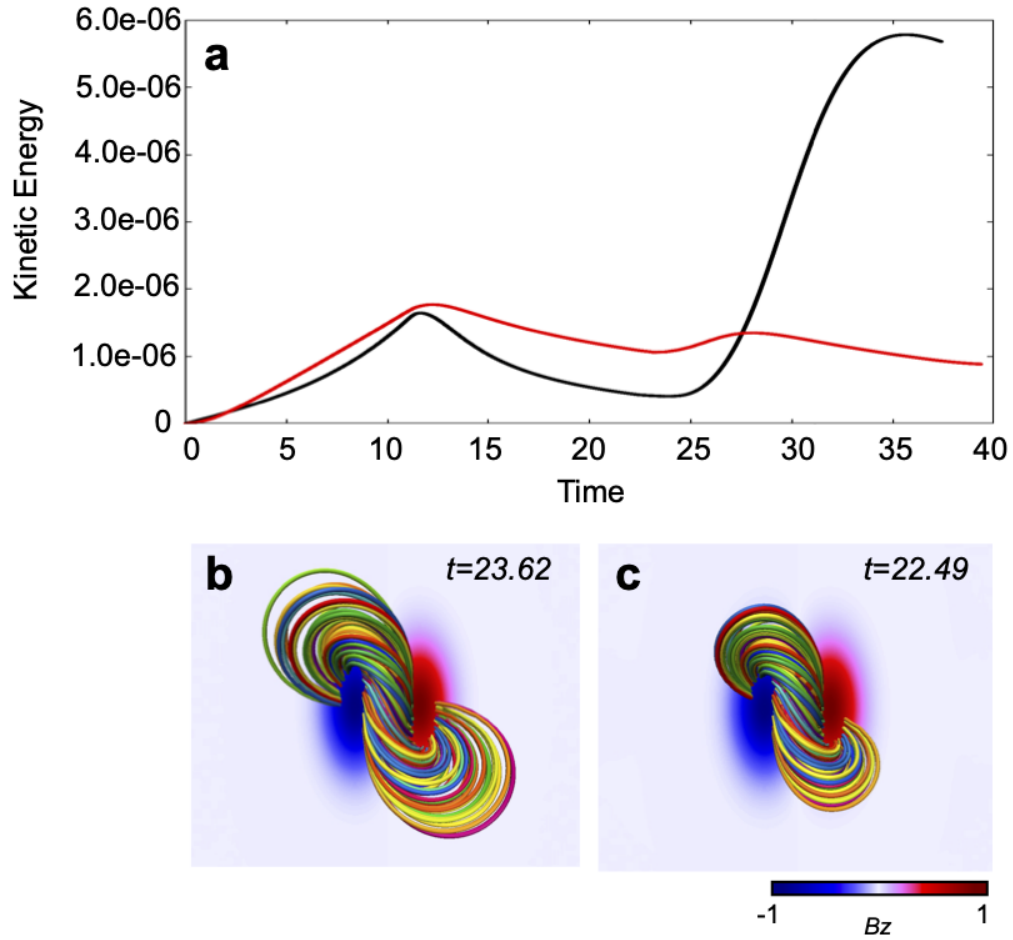


Fig. 21.— **a** The temporal evolution of the kinetic energy from $t = 0$ to the last time of the simulation for the ground-truth data shown in black and the data-driven simulation shown in red, respectively. This data-driven simulation was conducted with the same manner in TW-A2 and CV-A2. **b** Three-dimensional magnetic field lines in pre-erupting phase at $t=23.26$ for the ground-truth data. **c** Three-dimensional magnetic field lines in pre-erupting phase for the data-driven simulation.

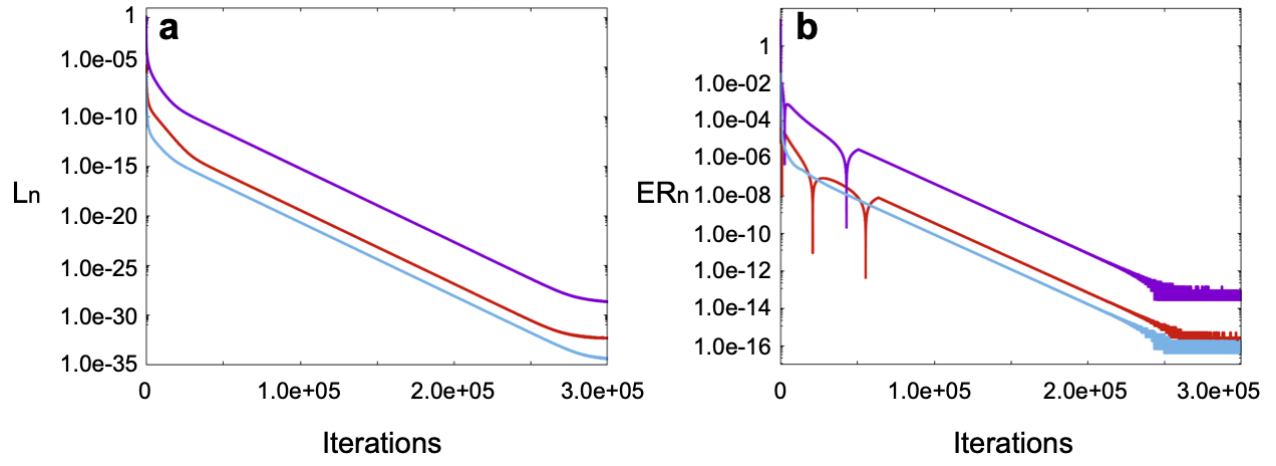


Fig. A1.— (a)-(b) Evolutions of L_n and ER_n , where $n=1,2,3$, during the iterations of each Poisson equation. Each color, red, purple, and blue represent $n=1$, $n=2$, and $n=3$, respectively.

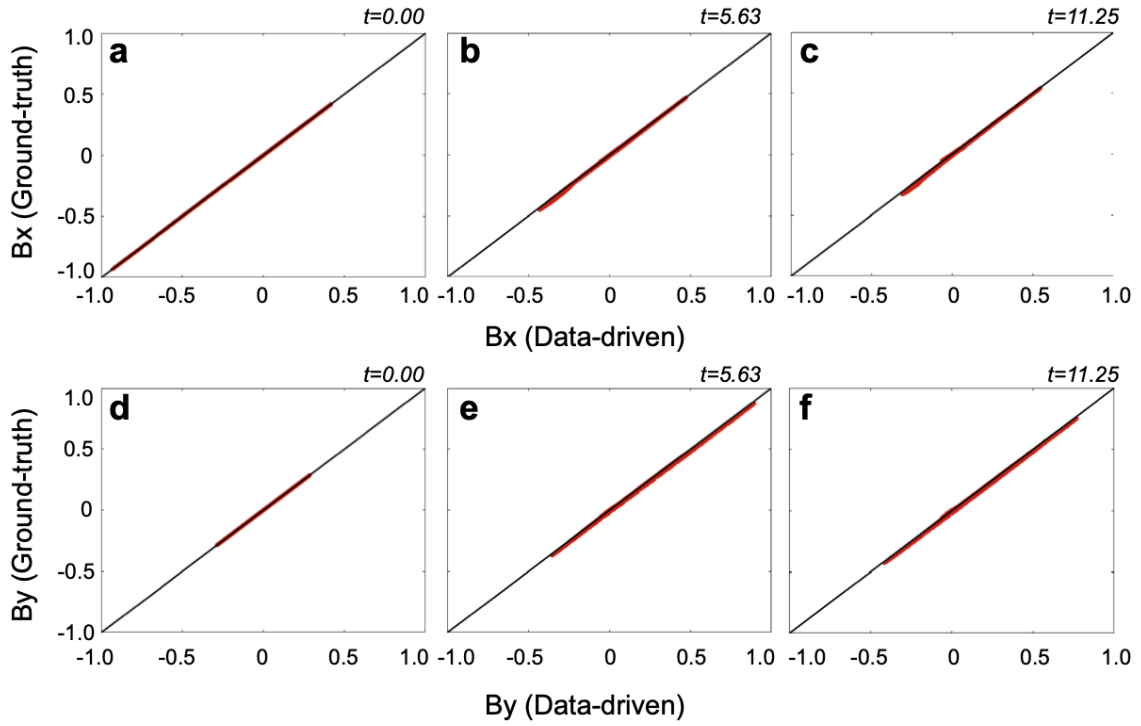


Fig. A2.— The scatter plot of the bottom magnetic fields by the ground-truth data vs. reproduced through the data-driven simulation. The upper and lower panels correspond to the distributions of B_x and B_y , respectively, at each time under the twisting motion. Note that the scatter plots on B_z are excluded because it does not changed during the evolution.

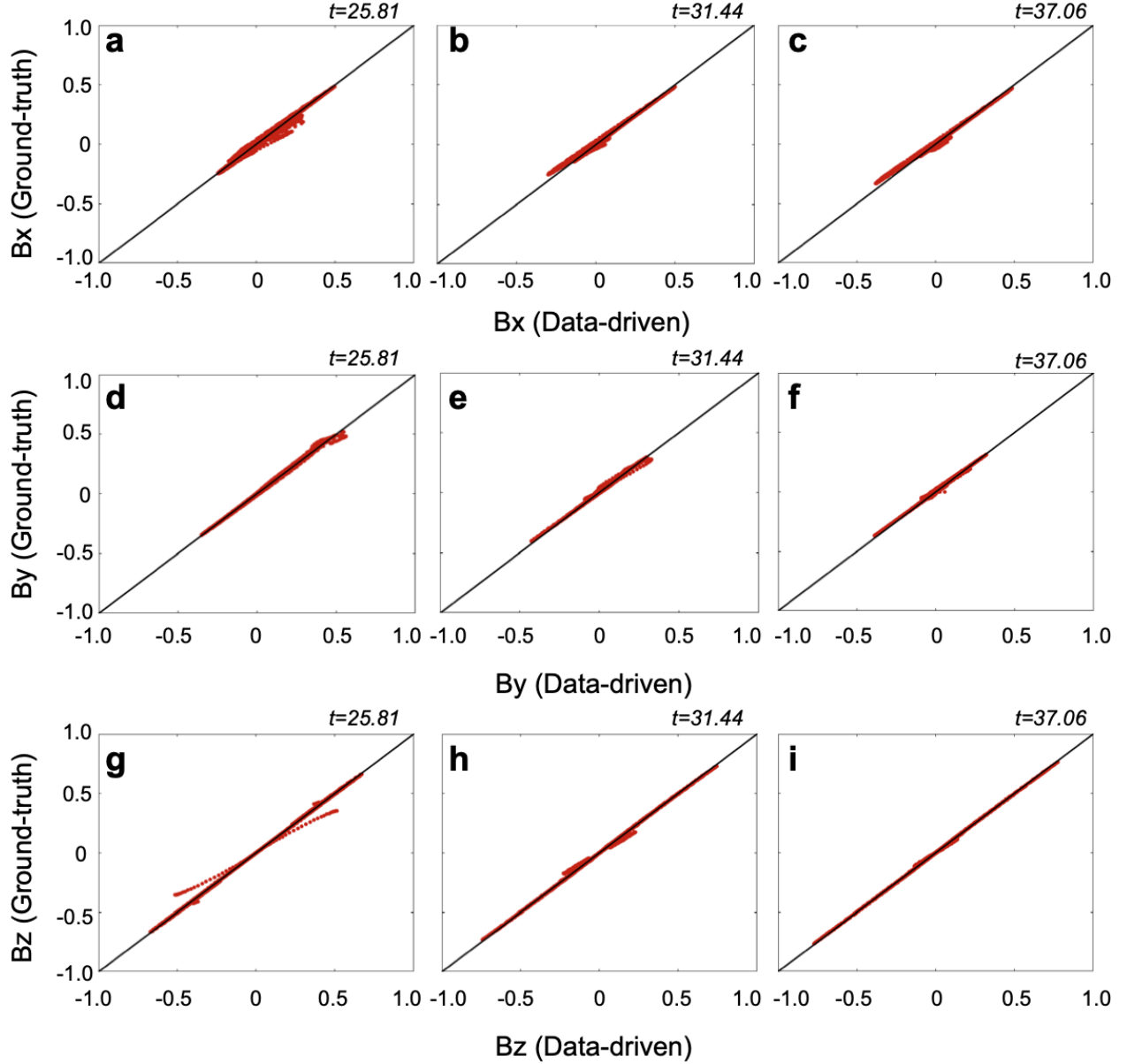


Fig. A3.— The scatter plot of the bottom magnetic fields from the ground-truth data vs. that reproduced through the data-driven simulation during the erupting stage, which are presented in the same format as in Fig.A2. The upper, middle and lower panels are the results regarding to B_x , B_y , and B_z components, respectively. Although these look a little scattered compared to Fig. A2, the correlation coefficients are over 0.99.

Table 1: All cases of the data-driven MHD simulation undertaken in this study are shown in the 1st column. The type of differential method and a way of updating for v_z at $k=1$ are listed in the 2nd and 3rd columns. Interpolation means that v_z at $k=1$ is derived from a linear interpolation with values at $k=0$ and $k=2$, *i.e.*, $v_z|_{k=1} = 0.5v_z|_{k=2}$. Because $v_z|_{k=0}=0$ is set in this study. Case, TW-A2D and CV-A2D are given with 2.5 times the temporal resolution of TW-A2 and CV-A2, respectively.

Case	Differential Method	v_z at $k=1$
TW-A0	A	Equation of motion
TW-A1	A	zero
TW-A2	A	interpolation
TW-A2D	A	interpolation
TW-B	B	interpolation
CV-A0	A	Equation of motion
CV-A1	A	zero
CV-A2	A	Interpolation
CV-A2D	A	Interpolation
CV-B	B	Interpolation